1 **Title:** Entorhinal cortex minimises uncertainty for optimal behaviour

2 **Authors:** Tobias Navarro Schröder[1,2], Benjamin W. Towse[3,4], Matthias Nau[1,2], Neil

3 Burgess[3,4], Caswell Barry[5], Christian F. Doeller[1,2,6,7]

4

5 **Affiliation:** (1) Kavli Institute for Systems Neuroscience, Centre for Neural Computation,

6 The Egil and Pauline Braathen and Fred Kavli Centre for Cortical Microcircuits, NTNU,

7 Norwegian University of Science and Technology, Trondheim, Norway; (2) Donders Institute

8 for Brain, Cognition and Behaviour, Radboud University, Nijmegen, the Netherlands; (3)

9 UCL Institute of Neurology, (4) UCL Institute of Cognitive Neuroscience; (5) UCL Research

10 Department of Cell and Developmental Biology, University College London, London, UK; (6)

11 St. Olavs Hospital, Trondheim University Hospital, Trondheim, Norway; (7) Max Planck

12 Institute for Human Cognitive and Brain Sciences, Leipzig, Germany

13

14 *Contact Information: t.navarroschroeder@ntnu.no or christian.doeller@ntnu.no

15

16 **Summary**

17 Minimizing spatial uncertainty is essential for navigation but the neural mechanisms remain

18 elusive. First, we show that polarising cues produce an anisotropy in the information

19 available to movement trajectories. Secondly, we simulate entorhinal grid cells in an

20 environment with anisotropic information and show that self-location is decoded best when

21 grid-patterns are aligned with the axis of greatest information. Thirdly, we expose human

22 participants to polarised virtual reality environments and confirm the predicted anisotropy in

23 navigation performance and eye movements. Finally, using fMRI we find that the orientation

24 of grid-like hexadirectional activity in entorhinal cortex is aligned with the environmental axis

25 of greatest information; and that this alignment predicted the anisotropy of participants'

26 spatial memory. In sum, we demonstrate a crucial role of the entorhinal grid system in

27 reducing uncertainty in the neural representation of self-location and find evidence for

28 adaptive spatial computations underlying entorhinal representations in service of optimising

29 behaviour.

30

31 Keywords: grid cells; computational modeling; virtual reality; fMRI; eye-tracking; spatial

32 navigation.

33

34

35 **INTRODUCTION**

1   Knowledge regarding one's position is inevitably incomplete and often incorrect. The

2   resulting uncertainty constrains the efficacy of behavioural outcomes and, as such, is an

3   important target for optimisation in decision making (Bach & Dolan, 2012; Daw & Dayan,

4   2014; Kiani & Shadlen, 2009; Knill & Pouget, 2004; Pouget, Beck, Ma, & Latham, 2013; van

5   Bergen, Ji Ma, Pratte, & Jehee, 2015; Yoshida & Ishii, 2006). Entorhinal grid cells are

6   thought to be a central part of a neural system for self-localisation, deployed in the service of

7   flexible navigation (Banino et al., 2018; Burak & Fiete, 2009; Bush, Barry, Manson, &

8   Burgess, 2015; Hafting, Fyhn, Molden, Moser, & Moser, 2005; McNaughton, Battaglia,

9   Jensen, Moser, & Moser, 2006). In humans, entorhinal fMRI-activity during virtual navigation

10   is modulated by movement direction. This modulation shows six-fold rotational symmetry (a

11   'hexadirectional signal') that has been proposed as a population signal of grid (Bellmund,

12   Deuker, Navarro Schröder, & Doeller, 2016; Doeller, Barry, & Burgess, 2010; Horner, Bisby,

13   Zotow, Bush, & Burgess, 2016; Julian, Keinath, Frazzetta, & Epstein, 2018; Kunz et al.,

14   2015; Nau, Navarro Schröder, Bellmund, & Doeller, 2018; Stangl et al., 2018). Moreover,

15   these hexadirectional signals in the entorhinal cortex have been associated with spatial

16   memory and navigation performance (Doeller et al., 2010; Kunz et al., 2015; Stangl et al.,

17   2018). However, it is an open question if the spatial grid code is subject to optimisation in

18   order to minimise the impact of environmental uncertainty on spatial decisions and

19   navigation.

20

21   The activity patterns of grid cells tile the environment with approximately equilateral

22   triangles, different modules of grid cells exhibiting different scales of tiling pattern, but

23   broadly similar orientations (Barry, Hayman, Burgess, & Jeffery, 2007; Stensola et al., 2012).

24   Computational work suggest that grid-patterns result from the integration of self-motion

25   information stabilised by sensory cues derived from the environment (Burak & Fiete, 2009;

26   N. Burgess, Barry, & O'Keefe, 2007; Bush, Barry, & Burgess, 2014; Giocomo & Hasselmo,

27   2008; Hardcastle, Ganguli, & Giocomo, 2015; McNaughton et al., 2006). Although grid cells

28   maintain their firing patterns in darkness (Hafting et al., 2005) (albeit transiently in mice

29   (Chen, Manson, Cacucci, & Wills, 2016)) and are relatively independent of discrete

30   environmental features their activity is clearly influenced by the sensory environment;

31   contact with a wall is sufficient to reset erroneous firing (Hardcastle et al., 2015) and grid-

32   patterns can be fragmented, polarised or distorted (Derdikman et al., 2009; Krupic, Bauza,

33   Burton, Barry, & O'Keefe, 2015; T. Stensola, Stensola, Moser, & Moser, 2015) by the

34   surrounding cues. Some of these changes result from manipulations made to an existing

35   environment (Barry et al., 2007; Stensola et al., 2012) and are likely transient (Barry,

36   Ginzberg, O'Keefe, & Burgess, 2012; Barry et al., 2007; Keinath, Epstein, &

37   Balasubramanian, 2017). However, in several cases, the observed effects are sustained and

1 appear to originate from an interaction between the grid-pattern and static sensory

2 environment, particular environmental geometry (Krupic et al., 2015; Stensola et al., 2015).

3 For example, grid-patterns recorded while rats first explore a square enclosure, initially align

4 with an axis parallel to the walls (Stensola et al., 2015) and subsequently rotate to favour a

5 relative angle of roughly 7.5°. Likewise, hexadirectional modulation of fMRI activity in the

6 human entorhinal cortex during visual exploration (akin to grid-cell-like activity in monkeys

7 during visual exploration (Killian, Jutras, & Buffalo, 2012)) shows anchoring to square

8 boundaries at 7.5° (Julian et al., 2018). Further, some visual grid cells in monkey (Killian et

9 al., 2012) show anchoring of activity to the stimulus display during free viewing (Meister &

10 Buffalo, 2018). However, it is not known if rotations and distortions of the grid are

11 maladaptive – a 'failed' attempt to generate a regular grid which might result in navigational

12 errors (Carpenter & Barry, 2016) – or, alternatively, if it confers an adaptive advantage for

13 self-localisation. More generally, the systematic changes in the spatial grid code following

14 manipulations of an animal's sensory environment promises to provide key insights into its

15 functional role in navigation and in coping with uncertainty in the environment.

16

17 Previously, we proposed that grid scale expansion, observed when rodents are placed in an

18 unfamiliar enclosure (Barry, Ginzberg, et al., 2012), is an adaptation to minimise the effect of

19 spatial decoding errors arising due to increased uncertainty in the grid system (Towse,

20 Barry, Bush, & Burgess, 2014). Here, we test if the effect of strongly polarising spatial cues

21 on grid orientation reflects an adaptive change to support spatial navigation. To this end, we

22 employ a combination of biologically inspired simulations, a virtual navigation task, and

23 fMRI-based estimate of entorhinal grid representations. Thereby we aim to shed new light on

24 the spatial computations underlying entorhinal grid representations and their role in

25 processing environmental uncertainty to guide navigation.

26

27 **RESULTS**

28 **Angular change is maximal during movement perpendicular to polarising cues**

29

30 To investigate the effects of uncertainty on grid cells andnavigation, we first determined the

31 presence of anisotropy of spatial information associated with the geometry of a polarised

32 environment. A major source of spatial information during motion is parallax, the apparent

33 change in direction to stationary points in the environment during movement. Below we

34 characterise an anisotropy of such angular change in polarised environments.

35

36 Suppose we have a circular arena of radius R centred on the origin, with a polarising cue at

37 distance L (Figure 1A). As an agent moves on a straight path b, we are interested in the

1   angle σ from the agent's heading to the cue, and how it changes when the agent moves. If

2   the cue is within the arena (L<R), then the maximal change in angle (π radians) occurs

3   when the agent moves towards and through the cue. If the cue is outside the arena (L>R),

4   and the length of the path is very short (i.e. in the limit b → 0) we can calculate the change in

5   angle $\delta\sigma$ to the cue (see Figure 1A, middle panel for example illustration with a longer path):

6

$$\frac{\delta\sigma}{b} = \frac{\sin\sigma}{a} \tag{1}$$

7

8

9   If the agent is on the x axis (i.e. $y = 0$) then we see that $\delta\sigma$ is proportional to $\sin\sigma$ which is

10   maximal for paths at $\theta = \frac{\pi}{2}$, i.e. movements perpendicular (90°) to the cue.

11   Hence, spatial information during movement is not isotropic across directions (this

12   conclusion holds on average for the entire arena). Specifically, angular change is maximal

13   during movement perpendicular to polarising cues. Spatial computations, such as Euclidean

14   triangulation, benefit from this parallax information and become more noise resilient (Figure

15   1 – figure supplement 1-3).

16

17   **Impact of environmental geometry on grid pattern may be adaptive**

18   Grid cells might play a role in determining self-location and planning movement trajectories

19   (Banino et al., 2018; Burak & Fiete, 2009; Bush et al., 2015; Hafting et al., 2005; Mathis,

20   Herz, & Stemmler, 2012; Towse et al., 2014). Biologically plausible simulations of self-

21   localisation with populations of grid cells suggest that, to maintain the most accurate

22   performance possible when spatial uncertainty is greater, the scale of grid cell patterns

23   should expand (Towse et al., 2014) as observed empirically in novel environments (Barry,

24   Ginzberg, et al., 2012). Here, we build on these previously developed models (Mathis et al.,

25   2012; Towse et al., 2014) by inquiring how position decoding using a population of grid cells

26   with coherent orientation is affected by anisotropy in spatial uncertainty (random

27   displacement of grid field). Grid cell ensembles with an axis set at angles from 0 to 30°

28   relative to the axis of greater uncertainty were simulated (due to the six-fold rotational

29   symmetry of the grid pattern, 30° is the largest possible angle between any line and the

30   closest of the pattern's axes). These simulations (see Materials and Methods) showed that

31   to achieve the most accurate position decoding, grid cells should have one of the three

32   pattern axes oriented at 30° to the axis of least spatial certainty (that is, as far misaligned as

33   possible; Figure 1C, Figure 1 – figure supplement 4-5). In control experiments, other

34   parameters of the grid cell system were varied and this result remained consistent across

35   these modifications (grid scale, firing rate, number of grid-cell modules; Figure 1 – figure

36   supplement 5). As established above, the axis of lowest spatial certainty corresponds to

1   moving parallel to the polarisation axis defined by the cues. This should lead to a larger

2   impact of noise on spatial computations, as well as to larger observed errors in spatial

3   memory responses. Thus this framework predicts that, in a circular environment polarised by

4   two cues grid cells should align one grid axis perpendicular to the polarisation axis.

5

6   **Effects of anisotropic information on spatial computations and behaviour**

7   Motion induced parallax is a source of navigation-relevant information (Gibson, 1958;

8   Raudies & Hasselmo, 2015) and lies at the heart of surveying unknown terrain for the

9   creation of spatial maps. Measuring angular changes to landmarks between different

10   observer locations is particularly powerful in combination with distance measurements. For

11   example, this underlies Euclidean triangulation (Crone, 1953; United States Department of

12   the Army, 1996). Biologically inspired simulations of Euclidean triangulation in polarised

13   environments corroborated that the impact of noise is minimised and that spatial information

14   is maximised for movement perpendicular to the polarisation axis (Figure 1 – figure

15   supplement 1-3; two-sided Wilcoxon signed-rank test: Z= 1026.42, p<0.001). Results were

16   robust within a plausible range of parameters. To test if the predicted anisotropy in spatial

17   information affect human behaviour, we conducted a behavioural distance estimation task

18   (N=20). After familiarisation with a sparse environment (Figure 2A, Figure 2 – figure

19   supplement 1) polarised by two cues defining an axis, participants navigated to a start

20   location from where they could initiate forward teleportation along one of three directions (-

21   30°, 0° and +30° relative to the polarisation axis; Angles < 90° were chosen to allow testing

22   of many distances with limited field-of-view, see Materials and Methods; Figure 2B; Figure 2

23   – figure supplement 1) and then give an estimate of the traversed distance (Figure 2A, see

24   Materials and Methods). As predicted, distance estimation was more precise when

25   participants did not move along the polarisation axis, but rather ±30° oblique to it (Figure 2C,

26    $T_{(19)}$ = 2.7, p=0.007; a similar pattern of results was observed for accuracy, see Figure 2 –

27   figure supplement 2). Hence, spatial navigation performance during more naturalistic free

28   virtual navigation could be expected to also reflect anisotropies in spatial information. We

29   conducted two such navigation tasks in different virtual environments with concurrent fMRI

30   scanning (N=26 and N=24), and a third one with concurrent eye tracking (N=34).

31   Participants freely navigated virtual environments with polarising, extra-maze cues (Figure

32   3). In fMRI experiment 1 and the eye tracking experiment, the environment was polarised by

33   configural cues, whereas in fMRI experiment 2 the environment was polarised by regular

34   cues (see Figure 3 and Materials and Methods). In each case they performed a continuous

35   object-location memory task (Doeller et al., 2010; Kunz et al., 2015) with 4 or 6 object-

36   location associations (see Materials and Methods): navigating to a target location, giving a

37   response, and receiving feedback, interrupted by occasional inter-trial-intervals when a

1   fixation cross was presented on a grey screen for 2 seconds (on average after every third

2   trial; range: 2-4). Object identity and location was randomised across participants (see

3   Materials and Methods). Despite a relatively sparse environment, participants successfully

4   learnt the object locations (Figure 3 – figure supplement 1). Participants could only translate

5   forward and rotate, but not move backwards, and in contrast to the distance estimation

6   experiment, allocentric movement direction was not fixed, which could affect an anisotropy in

7   spatial response errors. To avoid potential bias of the anisotropy measure, we matched the

8   number of trials in which participants faced (or moved) parallel (i.e. the Y dimension) and

9   perpendicular (i.e. the X dimension) to the polarisation axis ±45° at the time of the spatial

10 response (median difference in number of trials facing Y-facing X: experiment 1 = -4 ;

11 experiment 2 = 16; eye tracking experiment = 6.5). As predicted, participants' spatial

12 responses were more precise (median difference in drop error fMRI experiment 1= -1.3%;

13 fMRI experiment 2= -16.1%; eye tracking experiment= -1.5% error) perpendicular to the

14 polarisation axis than parallel with it, particularly in the sparse environment with only two

15 cues (Figure 3B. One-sided, one-sample Wilcoxon signed-rank test of participant's mean,

16 trial-wise (Y-X)/(X+Y) error fMRI experiment 1: p=0.2155, Z=0.79, n=26; fMRI experiment 2:

17 p=0.0067, Z= 2.47n=24; eye tracking experiment: p= 0.1870, Z=-0.89, n=34).Participants'

18 spatial memory performance hence indicates that movement directions parallel to the

19 polarisation axis might indeed be associated with low spatial certainty. This also suggest that

20 the degree of information differs between extra-maze cues, with the polarizing cues being

21 most informative. If correct, this should also be reflected in participants viewing behaviour,

22 leading to increased exploration of more informative cues. We therefore asked next if

23 participant's viewing behaviour would reflect the use of the polarisation axis. Notably, the

24 visual appearance of all cues was matched and cannot explain any potential viewing time

25 differences. We examined these potential differences in viewing times between cues using a

26 repeated-measures ANOVA. Indeed, average percent viewing time differed significantly

27 between cues (Figure 3 – figure supplement 1; $F_{(11)}$, p<0.0001, n=34). However, our specific

28 hypothesis was that the configural cues forming the polarisation axis (i.e. two pairs of cues

29 of opposite orientation) were the ones most viewed. A one-tailed paired t-test revealed that

30 the configural landmarks were indeed viewed longer than the ones orthogonal to the

31 polarisation axis ($T_{(33)}$=3.60, p=0.0005), which strongly suggests that they were key

32 elements for orientation – even though the anisotropy in spatial response errors did not

33 reach significance in the 12 cue environments.

34 If hexadirectional activity as an index of grid-cell-like representations would exhibit a

35 preferred orientation orthogonal to the polarisation axis, this would provide evidence for an

36 adaptive nature of the impact of environmental geometry on the grid pattern.

37

1 **Hexadirectional activity clusters orthogonal to polarisation axes**

2 To test environmental anchoring of the entorhinal activity in simple polarised environments,

3 we estimated hexadirectional entorhinal activity (Doeller et al., 2010; Horner et al., 2016;

4 Kunz et al., 2015). In brief, the method takes advantage of a six-fold periodic directional

5 modulation of fMRI activity in entorhinal cortex during virtual movement (see Materials and

6 Methods). The estimated orientations of hexadirectional entorhinal activity clustered

7 approximately perpendicular to an axis defined by the configural cues (Experiment 1, Figure

8 4) across participants (i.e. the absolute angle to the nearest 'grid axis' was approximately

9 30°, corresponding to maximum mis-alignment. Circular mean in 60°-space= 34°; Figure 4C-

10 D; N=26, circular V test for deviation from homogeneity perpendicular to the polarisation

11 axis: V=6.68, p=0.032). Note that low-level visual features were equal in all viewing

12 directions. A whole-brain analysis confirmed that activity in right entorhinal cortex was

13 increased for runs at periods of 60° aligned with the optimal orientation (Figure 5A-D, $T_{(25)}$

14 =4.44, small-volume FWE-corrected p=0.034), see Materials and Methods. In agreement

15 with grid-cell-like representations, runs aligned versus misaligned show largest activity

16 increase for 6-fold rotational symmetry but not for biologically implausible control models of

17 5- or 7-fold rotational symmetry (repeated-measures ANOVA: F(3,25) = 8.3, p < 0.001; Post-

18 hoc, paired t-tests with Holm-Bonferroni correction, * p<0.05). No other peaks remained

19 across the cerebrum even at more liberal thresholds (p<0.001 uncorrected; T>3.45) and

20 neither was there a significant circular clustering of hexadirectional activity in 2 control

21 regions (mammillary bodies, which are close to the hippocampal formation: V test: V=3.33,

22 p=0.822; right, primary visual cortex: V test: V=0.10, p=0.489; See Materials and Methods).

23

24 To test if the environmental anchoring depends on the configural cues, we scanned another

25 group of participants in an environment with a non-configural, polarisation axis consisting of

26 only two extra-maze cues. The estimation direction of hexadirectional activity again

27 clustered perpendicular to the polarisation axis (circular mean in 60°-space= 32.28°; Figure

28 6) replicating the findings from the first experiment (i.e. the absolute angle to the nearest

29 axis was approximately 30°, corresponding to maximum mis-alignment; N=24, circular V

30 test: V = 5.95, p=0.043; Figure 6). Sampling of running directions could not explain these

31 effects in either experiment (Figure 3 – figure supplement 1). In sum, the results from fMRI

32 experiment 1 and the replication in fMRI experiment 2 provide converging evidence that the

33 preferred orientation of hexadirectional activity in entorhinal cortex depends on navigation-

34 relevant, polarising cues, independent of the specific type of cue (configural or non-

35 configural). The orthogonal arrangement of hexadirectional activity is in agreement with

36 optimal activity patterns of grid cells for self-localisation, suggesting that the impact of

37 environmental geometry on grid cells may be adaptive.

1

2 **Behavioural anisotropy is linked to hexadirectional orientation**

3 To test a potential relationship between the anisotropy in spatial memory performance (see

4 above) and hexadirectional activity, we pooled the data from fMRI experiment 1 and 2. This

5 metric showed a positive correlation with the angular offset of hexadirectional activity from

6 the polarisation axis of the environments (Figure 4D, Figure 6C) across participants (Figure

7 6D; one-sided, Spearman's correlation with pooled data of experiment 1 and experiment 2.

8 N=50: R=0.291, p=0.020). The positive relationship indicates that participants with a more

9 orthogonal orientation of hexadirectional activity were relatively more precise in placing

10 objects on the X dimension than the Y dimension). This association provides further

11 evidence for an adaptive nature of changes in grid-cell-like representations caused by

12 environmental geometry.

13

14

15 **DISCUSSION**

16 To navigate the world around us we often have to orient ourselves using noisy and

17 incomplete information. For example, landmarks can be occluded, or very far away, or

18 change their relative direction during movement. The neural systems involved in optimal

19 spatial decision making (i.e. to determine where you are and where you want to go) in face

20 of changing sensory information are likely to involve entorhinal grid cells, given their

21 integration of angular and distance information and their proposed role in self-localisation

22 and navigation (Bush et al., 2015; Hafting et al., 2005; H. Stensola et al., 2012; Towse et al.,

23 2014). However, the computational mechanisms underlying the grid system remain

24 unknown. Perturbations of the grid pattern in response to environmental geometry (Krupic et

25 al., 2015; T. Stensola et al., 2015) could be adaptive or rather maladaptive for spatial

26 navigation. Distinguishing between these two options would inform a potential role of grid

27 cells in coping with spatial uncertainty and guiding navigation.

28

29 To shed light on these issues we combined biologically inspired, computational modelling,

30 behavioural testing, and fMRI-based proxy measures of grid-cell-like population activity. We

31 designed virtual environments where we predicted anisotropies in spatial information across

32 different moving directions. In particular, we focused on the angular change to stationary

33 cues during movement. In line with our predictions, estimation of movement distance was

34 least precise when participants moved along a polarisation axis. Likewise, spatial memory

35 performance in the free-navigation, object-location memory task of fMRI experiment 2

36 showed relatively larger errors parallel to a polarisation axis (i.e. anisotropy). This anisotropy

37 in spatial memory was not significantly different from zero in fMRI experiment 1 and the eye

1 tracking experiment, which could be explained by a more even distribution of spatial

2 uncertainty across movement directions in the environment with 12 cues. Here, differences

3 in parallax information arise only through the 'second order' configural cues, rather than

4 single cues, and the eye tracking experiment confirmed that those were attended to for a

5 longer time than others. To test the theoretical implications of anisotropic spatial information

6 on a system of grid cells, we used biologically inspired simulations. We demonstrate that the

7 most accurate representation of self-location is obtained when grid-patterns are misaligned

8 at 30° with the polarisation axis, reflecting an alignment of the grid pattern with the axis of

9 highest spatial information. fMRI-based estimates of hexadirectional activity in the entorhinal

10 cortex, reflecting putative grid-cell representations (Bellmund et al., 2016; Doeller et al.,

11 2010; Julian et al., 2018; Kunz et al., 2015; Nau et al., 2018; Stangl et al., 2018), revealed

12 consistent orientations across participants in two independent experiments. Importantly,

13 these effects cannot be explained by the presence of objects during part of each trial, since

14 their locations were randomised and the two fMRI experiments had different numbers of

15 objects (6 and 4). As predicted, the phase of the hexadirectional signal in entorhinal cortex

16 aligned with the axis of highest spatial information - the optimal grid orientation for decoding

17 self-location. Importantly, the angular offset of hexadirectional activity from the polarisation

18 axis correlated negatively with the anisotropy in spatial memory performance. This might

19 result from different navigation strategies that participants used, for example focussing on

20 subtle landmarks such as differences in the grass on the ground or on the texture of the wall,

21 Taken together, our results provide evidence that the effects of environmental geometry on

22 the grid system are adaptive and angular change to stationary cues play a central role in the

23 computations underlying the grid system. These computations may be sensitive to

24 polarisation axes defined by cues rather than information provided by environmental

25 boundaries per se.

26

27 Our findings are in agreement with reports showing that entorhinal fMRI activity correlates

28 with Euclidean distance to a goal location (Howard et al., 2014) and the proposal that grid

29 cells might enable goal-directed vector navigation (Burak & Fiete, 2009; Bush et al., 2015;

30 Erdem & Hasselmo, 2013; Kubie & Fenton, 2012; Mathis, Herz, & Stemmler, 2013;

31 Sreenivasan & Fiete, 2011; Stemmler, Mathis, & Herz, 2015; Towse et al., 2014).

32 Interestingly, both angular and distance information that is needed for triangulation can be

33 derived from either visual or proprioceptive and vestibular cues. For example, visually

34 modulated cells in the rat posterior-parietal cortex signal the egocentric cue direction

35 (Wilber, Clark, Forster, Tatsuno, & McNaughton, 2014) and head-direction cells in the

36 entorhinal cortex and other regions realign to visible cues, but also function without vision

37 and rely on vestibular information (Taube, 2007). On the other hand, distance information

1   can be inferred visually from the relative size of objects and cues (Gibson, 1958) or is based

2   on proprioceptive and timing information during movement, both of which modulate grid cell

3   activity (Kraus et al., 2015). Hence, triangulation for navigation could bridge different sensory

4   modalities. Furthermore, it combines egocentric cue directions and distance information to

5   infer map-like, survey representations of the environment, thereby naturally integrating

6   egocentric and allocentric reference frames, which are not mutually exclusive and can work

7   in parallel and across brain regions (N. Burgess, 2006; Epstein, 2008; Wilber et al., 2014).

8

9   An exciting avenue for future studies is to explicitly examine the effect of anisotropic spatial

10   uncertainty on rodent grid-cell firing. It is known that grid cell firing exhibits plasticity,

11   regularising and reorienting incrementally with continued experience of an enclosure (Barry

12   et al., 2007; Barry, Heys, & Hasselmo, 2012; Carpenter et al., 2015; Stensola et al., 2015).

13   Our results suggest that these changes likely optimise the grid-code, allowing for an

14   increasingly accurate representation of self-location. However, the physiological and circuit

15   mechanisms that facilitate and direct this process are currently unknown. Theoretically, a

16   number of authors have considered the impact of noise in grid cell coding of self-location

17   and its implications for the capacity and error-tolerance of the entorhinal spatial

18   representation (Burak & Fiete, 2009; C. P. Burgess & Burgess, 2014; Navratilova, Giocomo,

19   Fellous, Hasselmo, & McNaughton, 2012). However, to the best of our knowledge, we have

20   provided the first theoretical and practical account of anisotropic spatial uncertainty on the

21   grid system. It remains to be seen if such asymmetries, which are likely a common feature of

22   the environment (Hardcastle et al., 2015), exert more wide-ranging influences on grid-firing;

23   distorting the grid-pattern or changing the relative scales of different grid modules; or might

24   also impact grid-like coding of non-spatial information. In conclusion, our results are

25   consistent with an adaptive and flexible role of grid cells in self-localisation and navigation.

26   This opens up the exciting possibility for a deeper understanding of fundamental neural

27   building blocks of cognition and behaviour.

28

1

2 **Materials and Methods**

3

4 ***Simulation of Euclidean triangulation***

5 To test the impact of stochastic fluctuations or noise on triangulation accuracy, we

6 implemented the following simulation in Matlab (2012b, The MathWorks Inc.,

7 Massachusetts). Triangles were formed by two points representing start and end points of a

8 straight path in the horizontal plane (e.g. observer locations at time point 0 and time point 1)

9 and one of two polarising, stationary cues. Triangulation was based on the sine rule

10 according to:

11 $$c = b * sin\,(\sigma)/\,sin\,(\delta\sigma) \qquad\qquad (2)$$

12 where *c* is the unknown side (distance to the cue at the end point; Figure 1 – figure

13 supplement 1), *b* the known side (distance travelled), σ the angle to the cue at the start point

14 and $\delta\sigma$ the angular change to the cue between start and end point.

15 Path orientation (azimuth) was varied in steps of 1°, path length remained constant and each

16 path was centred on the origin of the coordinate system. Hence, the start and endpoints of

17 different paths mapped onto a circle. This ensured that the mean distance of different paths

18 to one or multiple cues remained constant. Before the triangulation iterations, random noise

19 was added to the known side and the two distance angles. The error in side length had a

20 mean absolute deviation of roughly 5% the original length (based on typical human distance

21 errors during walking (Elliott, 1987)) and was drawn from a Gaussian distribution with mean

22 0 and a sigma of path length of 15.95. The absolute angular error for a single angle was 5°

23 on average (drawn from a von Mises distribution with mean 0 and a sigma of 6.26) and 15°

24 on average for the absolute cumulative error across all three angles of a triangle. This error

25 rate was based on the mean, absolute angular error observed in humans performing a

26 triangle completion task in virtual reality, which involved pointing to a start location after an

27 outward path with two turns (Wolbers, Wiener, Mallot, & Büchel, 2007).

28

29 *Triangulation measurements: noise resilience.* Triangulation was repeated for all sides of a

30 triangle using the known base *a*. If the inferred side was the base (the path), triangulation

31 was repeated with both remaining sides serving as the known side and the two results were

32 then averaged. Dual triangulation for the base was done to avoid biased results due to the

33 selection of any one of the remaining sides. Note that the length of the remaining sides was

34 not constant and changed in opposite directions for different path angles, potentially

35 affecting the noise resilience measure at different path angles. This was not a problem in the

36 reverse case, because the base (side *a*) had constant length. The triangulation error for the

37 3 sides was computed as the absolute difference in the original side length and the length

11

1   based on triangulation with noisy input parameters. The 3 error rates were then averaged for

2   further computations and the assessment of noise resilience across paths (Figure 1 – figure

3   supplement 1-3). Furthermore, the distance between the most proximal cue to the centre of

4   each path (the middle of the base of a triangle) was always equal to the length of the path,

5   with the exception of Figure 1 – figure supplement 33 that shows the effects of different path

6   lengths and different noise levels. In other words, usually the path length was half the length

7   of the polarisation axis. Triangulation to additional cues was performed for a given path

8   angle if these were within ± 90° (determined from the centre of a path) to emulate a limited

9   field-of-view. This meant that cues in only that half of the environment were used for

10   triangulation that was faced on a given path (1 point in Figure 1 – figure supplement 1).

11

12   *Triangulation measurements: triangle quality.* The quality measure for triangle shape

13   (triangle area divided by the sum of squares of side lengths; Figure 1 – figure supplement 1

14   light blue curve) was modified from (Bank & Smith, 1997) who describe optimization of finite

15   element triangulations in the generation of meshes.

16

17   **Computational models of grid cell systems**

18

19   **Grid cell system model**

20   Spiking activity of a population of grid cells, organised into 4 (except where otherwise

21   specified) discrete modules by spatial period size, was modelled in a two-dimensional

22   circular environment of radius 50cm using Matlab v.8 (Mathworks). Spatial periods or grid

23   scales, λ_i, were determined as a geometric sequence beginning with λ_1 = 25cm and

24   increasing with a scale factor of 1.4 (except where otherwise specified). Tuning curves for

25   each grid scale λ_i were generated with locations of grid nodes specified as a regular

26   triangular grid and expected firing rate at each location determined by a Gaussian

27   distribution centred on the nearest node:

28
$$\alpha_{i,j}(x,y) = f_{max}e^{-\frac{d^2}{2\sigma_i^2}}$$

29   where *j* specifies a particular cell, *d* is the distance from (x,y) to the nearest grid node, f_{max}

30   the maximum firing rate (constant across the population; 10Hz except where otherwise

31   specified), σ_i the tuning width of the grid fields ($\sigma_i = 3\lambda_i/(20\sqrt{\log_e 100})$ following (Mathis et

32   al., 2012).

33

34   Within each of the 4 modules, M = 195 offset tuning curves were distributed in a 13 × 15

35   rectangular grid via translations of this original tuning curve, as well as adding a random

36   translation common to all grids in the module. This resulted in a total of 1560 grid cells in a

1   system. Grid tuning curves could also be rotated to specified orientations; all grid tuning

2   curves always shared a common orientation. All these transformations were performed

3   using cubic interpolation.

4

5   In each iteration of the model, the true position (x, y) was specified as the centre of the

6   circular environment (0, 0). To model uncertainty, Gaussian noise, with standard deviation

7   varied independently in x and y, was generated separately for each module and added to (x,

8   y), to yield a noisy position estimate (x + $\varepsilon_{x,i}$, y+ $\varepsilon_{y,i}$). Anisotropic uncertainty was produced by

9   independently varying the standard deviations of $\varepsilon_{x,i}$ and $\varepsilon_{y,i}$ between 0 and 5. All cells within

10   a module therefore received the same noisy position input, but cells in different modules

11   received different input. Thus cell firing rate was now modulated according to α_i (x + $\varepsilon_{x,i}$, y+

12   $\varepsilon_{y,i}$).

13

14   The signal extracted from the grid cell system was the number of spikes, *k*, generated by

15   each neuron during a finite read-out period, *T* = 0.1s (the approximate length of a theta

16   cycle) – i.e. a population response *K = (k₁, …, kₙ)*. We assume the decoding cannot take the

17   added noise into account in any way, so that given a position *x* the probability of observing

18   the response *K* in time T, following (Mathis et al., 2012), is taken to be:

19
$$P(\boldsymbol{K}|x,y) = \prod Poisson\left(k_{i,j}, T\alpha_{i,j}(x,y)\right) = \prod \frac{\left(T \times \alpha_{i,j}(x,y)\right)^k}{k!} \times e^{-T\alpha_{i,j}(x,y)}$$

20

21   where $\alpha_{i,j}(x,y)$ is calculated by cubic interpolation from the tuning curve. From the population

22   response *K*, we can decode position as the maximum likelihood estimate of *(x, y)*, that is

23   *x̂,ŷ(K)*. Given the initial assumption that all positions within the environment are uniformly

24   likely,

25

26
$$\hat{x}, \hat{y}(\boldsymbol{K}) = \max P(x,y|\boldsymbol{K}) = \max P(\boldsymbol{K}|x,y)$$

27

28   Thus *x̂,ŷ(K)* may be closely approximated by calculating *P(K|x,y)* for a sufficiently finely

29   spaced uniform sample of *x* and *y* values across the environment, and selecting the values

30   of x and y which yield the greatest *P(K|x,y)*. We used a spatial bin size of 0.5 cm. Where two

31   or more solutions yielded the same maximal *P(K|x,y)* (i.e. decoding was ambiguous), one

32   was randomly selected (Mathis et al., 2012; Towse et al., 2014).

33

34   *Assessing grid system performance*

35   For each combination of levels of uncertainty in x and in y, we assessed the performance of

36   grid systems whose patterns were orientations to these x-y axes from 0° to 30° at intervals

1 of 2.5°. For each case, five experiments each consisting of 15,000 iterations of this

2 procedure were performed. In each of these five experiments, the square grid across which

3 the environment was sampled to produce tuning curves was set at a different orientation to

4 the environment's Cartesian axes, in order to control for any effect of uneven sampling (the

5 orientations were 0° and 4 orientations randomly selected and then used across all

6 conditions). The results of equivalent pairs of uncertainty levels (e.g. standard deviation

7 respectively in x and y of 0 and 5 cm, and 5 and 0 cm) were combined to total 2 × 5 ×

8 75,000 = 150,000 iterations. Using these, accuracy of decoding was assessed via the

9 approximated maximum-likelihood estimate square error, or MMLE, based on the square

10 errors of position decoding:

11
$$MMLE \approx \frac{1}{75000} \sum_{c=1}^{75000} \left(0 - \hat{x}(\boldsymbol{K}_c)\right)^2 + \left(0 - \hat{y}(\boldsymbol{K}_c)\right)^2$$

12

13 ***Neuroimaging,behavioural- and eye-tracking experiments***

14 ***Participants***

15 *FMRI experiment 1*. 26 participants took part in the study (12 females, age range: 19–36,

16 mean age: 23 years). Materials and Methods were approved by the local research ethics

17 committee (ethics committee University Duisburg-Essen, Germany and CMO region

18 Arnhem-Nijmegen, NL). Written informed consent was obtained from each participant.

19

20 *FMRI experiment 2*. 25 participants took part in this study (11 females, age range: 18-32,

21 mean age: 24 years). One participant was excluded from the analysis due to poor

22 performance (i.e. 55 trials with no location response within 30 seconds of the respective trial,

23 more than a standard deviation above the mean). Materials and Methods were approved by

24 the local research ethics committee (CMO region Arnhem-Nijmegen, NL). Written informed

25 consent was obtained from each participant.

26

27 *Behavioural experiment.* 20 participants (11 females, age range: 18-24, mean age: 20 years)

28 participated in the behavioural experiment. Materials and Methods were approved by the

29 local research ethics committee (CMO region Arnhem-Nijmegen, NL). Written informed

30 consent was obtained from each participant.

31

32 *Eye tracking experiment:* 36 participants (15 females, age range: 18-63, mean age: 26)

33 participated in the experiment. Two participants aborted the experiment early, because of

34 VR-induced nausea, and their data was excluded from all analyses. Materials and Methods

14

1   were approved by the local research ethics committee (CMO region Arnhem-Nijmegen, NL).

2   Written informed consent was obtained from each participant.

3

4

5   ***FMRI acquisition.***

6   *FMRI experiment 1*. Blood-oxygenation-level-dependent (BOLD) T2*-weighted functional

7   images were acquired on a 7T Siemens MAGNETOM scanner (Siemens Healthcare,

8   Erlangen, Germany) using a three dimensional echo-planar imaging (3D EPI) pulse

9   sequence (Poser, Koopmans, Witzel, Wald, & Barth, 2010) with a 32-channel surface coil

10   with the following parameters: TR = 2.7 s, TE = 20 ms, flip angle = 14°, voxel size 0.9 × 0.9

11   × 0.9 mm, field of view (FoV) = 210 mm in each direction, 96 slices, phase encoding

12   acceleration factor = 4, 3D acceleration factor = 2. The scanning session was subdivided

13   into EPI acquisition blocks of 210 volumes each. The majority of participants performed 5

14   blocks over the course of approximately 55 minutes. Deviations from the 5 blocks in a few

15   participants were due to technical problems or interruptions on behalf of the participants (3

16   participants had 4 blocks, 2 participants 6 blocks). In addition, T1-weighted structural images

17   (MP2RAGE; voxel size: 0.63 mm isotropic) and a field map (gradient echo; voxel size: 1.8 x

18   1.8 x 2.2 mm^3) were acquired. Results of an entirely unrelated, task-independent whole-

19   brain connectivity analysis of data from experiment 1 have been described in a previous

20   report (Navarro Schröder, Haak, Zaragoza Jimenez, Beckmann, & Doeller, 2015).

21

22   *FMRI experiment 2*. BOLD T2*-weighted functional images were acquired on a 3T Siemens

23   Trio scanner (Siemens Healthcare, Erlangen, Germany) using a three dimensional echo-

24   planar imaging (3D EPI) pulse sequence (Poser et al., 2010) with a 32-channel surface coil

25   with the following parameters: TR = 1.8 s, TE = 25 ms, flip angle = 15°, voxel size 2 × 2 × 2

26   mm, field of view (FoV) = 224 mm in each direction, 64 slices, phase encoding acceleration

27   factor = 2, 3D acceleration factor = 2. Each scanning session consisted of an EPI acquisition

28   block of 1031 volumes on average (range: 661-1200). In addition, T1-weighted structural

29   images (MPRAGE; voxel size, 1 mm isotropic; TR, 2.3 s) and a field map (gradient echo;

30   voxel size, 3.5 x 3.5 x 2 mm^3) were acquired.

31

32   ***Experimental tasks***

33   *FMRI experiment 1*. Participants freely navigated a 3D virtual reality environment with a

34   modified version of the arena from the studies by Doeller and colleagues (Doeller et al.,

35   2010; Kunz et al., 2015) (Figure 3A) using a 4-button controller. UnrealEngine2 Runtime

36   software (Epic Games) was used to generate the virtual reality task. Instead of two

37   orthogonal axes that are formed by the walls of square enclosures (as in (Krupic et al., 2015;

15

1   Stensola et al., 2015)) we opted for the simplest case of a single axis, which was determined

2   by extra-maze cues in a circular arena. We hypothesized that the orientation of grid

3   representations would be coherent across participants, as shown in rats moving through

4   square environments, and that this orientation would be determined by the amount of spatial

5   information obtained on movement paths of such orientation. The environment consisted of

6   a circular arena with 12 extra-maze cues, 6 upright and 6 inverted triangles. Two pairs of

7   neighbouring triangles of different orientation comprised the two configural cues on opposite

8   sides of the arena that defined a polarisation axis. To control for possible visual effects on

9   our direction-related analysis, we designed the colour textures for the extra-maze cues in

10 such a way, that the low-level visual features remained equal across cues. Each triangle had

11 a red, green and blue corner, arranged in 1 of 6 possible constellations. The arrangement of

12 textures was randomised across participants. Participants performed a self-paced object-

13 location memory task that involved collecting and replacing six everyday objects to locations

14 that were randomised across participants. Participants collected each object from its

15 associated location once during an initial phase, by running over it. Navigation was not

16 interrupted during the transitions between trials to enable more natural (ecologically valid)

17 continuous navigation. In each subsequent trial they saw an image (cue) of one of the

18 objects in the upper part of the screen and had to move to the object's associated location

19 and press a button (replace phase). After this response, the object appeared in its

20 associated position and participants collected it again (feedback phase). After an average of

21 3 trials (range 2-4 trials), a fixation cross on a gray background was presented for 4 seconds

22 (inter-trial-interval, ITI). Object locations were randomised across participants. Since the task

23 was self-paced, the number of trials varied across participants (range: 94-253; mean: 179).

24 Prior to the fMRI experiment, participants performed a similar object-location task with

25 different objects in a different virtual environment outside the scanner to familiarise

26 themselves with the task demands.

27

28 *FMRI experiment 2.* Participants freely navigated the same virtual environment as used in

29 fMRI experiment 1, but with only two extra-maze cues on opposite sides of the arena that

30 defined a polarisation axis (Figure 3A). Participants performed the same object-location

31 memory task described above, except that 4 objects were used instead of 6. Participants

32 performed an average of 117 trials (range: 63-179). Prior to the fMRI experiment,

33 participants performed a similar object-location task with different objects and a different

34 virtual environment outside the scanner to familiarise themselves with the task demands.

35

36 *Behavioural experiment.* Participants freely navigated a virtual reality environment (Figure

37 2A, Figure 2 – figure supplement 1) by using four buttons on a keyboard to move in the four

1   cardinal directions and the mouse to change horizontal viewing direction. The virtual
2   environment was displayed at 1680x1050 pixel resolution and 60 Hz refresh rate
3   approximately 40cm in front of the participants' eyes. They were teleported between varying
4   start and end locations at one of three possible angles and performed a distance estimation
5   task. The environment was a 'pitch black' space with otherwise only three distinguishable
6   elements. First, it included a background consisting of a white dashed line oriented
7   horizontally and projected at infinity. This background provided minimal visual information to
8   perceive rotational movements as well as motion parallax of a cue viewed from different
9   angles. Second, a cue, consisting of a red circle, was displayed vertically on a fixed location.
10 Third, a red circle indicated the start location of each path with an arrow pointing in the
11 direction of the goal location. The rationale behind using a visually sparse environment and
12 teleportation to the goal location was to prevent the use of other distance cues, such as cue
13 size (e.g. patches of grass or a boundary) or an estimate of 'time-of-flight', respectively. This
14 ensured that the change in size of the cue and the change in angle and motion parallax to
15 the cue from start to the end of a path was the sole means by which the distance estimation
16 task could be performed correctly. Prior to the experiment, participants performed a similar
17 distance estimation task in a different virtual environment to familiarise themselves with the
18 task demands. At the beginning of the behavioural experiment, participants were instructed
19 to approach the cue in order to familiarise themselves with its location and distance.
20
21 The trial structure was as follows: Participants were instructed to navigate to the starting
22 point. Once they reached the starting point, their movement was restricted to rotations and
23 the message 'click right mouse button to teleport ahead' was displayed (orientation phase
24 one). Participants could self-initiate teleportation to the goal location by a mouse-click and
25 orienting towards the pointing direction of the arrow, at which point the view was frozen and
26 teleportation commenced 2 seconds later. After teleportation to the goal location, the start
27 location became invisible (the red circle with arrow disappeared), movement remained
28 restricted and only rotations were possible and the message 'click right mouse button to give
29 response' was displayed (orientation phase two). Participants could self-initiate the response
30 phase. Then, a horizontally oriented window was displayed together with the message
31 'indicate distance (left = minimum, right = maximum)' and participants could move the
32 mouse to slide a bar inside the window to indicate how far they thought they were being
33 teleported. The range of possible responses was 0 virtual units (vu) to 6000 vu. For
34 comparison, the arena diameter used in the fMRI studies was 9500 vu for the inner
35 boundary and the length of the polarisation axis (i.e. the distance between opposing, extra-
36 maze cues) was 12064 vu. The range of teleportation distances was 500 vu to 5500 vu
37 (mean = 2742 vu). The response was finalised by another mouse click and subsequently,

1   feedback in the form of smiley faces was given for 2 seconds. The color of a smiley for a

2   response error < 2% of the correct distance was green, light green for an error < 4 %, yellow

3   for an error < 8 %, orange for an error < 16% and red otherwise. During this feedback

4   phase, participants could still move the response bar to see other response-to-feedback

5   mappings (i.e. the smiley associated with a given horizontal pixel location). Once the

6   feedback disappeared, participants were able to freely navigate again. At the beginning of

7   about 50% of trials (determined pseudo-randomly), participants were placed to a point in

8   front of the start location to speed up the experimental procedure (i.e. to reduce navigation

9   time from a goal location to the start location of the subsequent trial) and thereby increase

10   the number of trials. In addition, the orientation phase 1 and 2 were restricted to 6 seconds

11   and the response phase to 4 seconds indicated through the display of a timer. If the time

12   limit was reached, 'Time is up! This trial is invalid' was displayed on a red background and

13   no response was recorded. Teleportation distances and teleportation directions were

14   pseudo-randomly determined on each trial. Teleportation directions were either 0°

15   (approaching the cue on a straight line), -30° or +30°. The location of the cue was at (x = 0

16   vu , y = 8500 vu) and following the approach of the simulations, all paths were centered on

17   the origin of the coordinate system. However, this would provide a relative advantage to the

18   parallel condition. The size of the cue directly reflects its distance to the observer, which

19   becomes particularly apparent at close proximity. In the -30° and the +30° conditions, the

20   goal location is always further away from the cue compared to the 0° condition at equal

21   teleportation distances. Furthermore, the independent measure (teleportation distance) is

22   linearly associated with goal-to-cue distance only in the 0° condition. To avoid bias due to

23   unequal goal-to-cue distance, we equalized this measure by subtracting the difference

24   across conditions (at equal teleportation distances). In effect, this shifted the teleportation

25   paths in the 0° condition backwards by a given amount (Figure 2B). Due to a limited field-of-

26   view of 85°, testing of large path offsets of e.g. 90° was not feasible. The task duration was

27   limited to 30 minutes in which participants performed an average of 129 self-paced trials

28   (range: 52-238). Prior to the main task, participants performed a training version of the task

29   in a richer virtual environment with a comparable trial structure where the length of the path

30   was not traversed by teleportation but rather through guided movement.

31

32   *Eye tracking experiment:* During a magnetoencephalography study (MEG; data are subject

33   of an independent report), participants performed the same task in the same virtual

34   environment as in fMRI experiment 1 (i.e. the environment with 12 cues). However, they had

35   to learn the locations of 8, instead of 6 objects. Simultaneously, gaze position and pupil area

36   of the left eye were monitored with an infrared-based Eylink 1000 eye tracking system at

37   1200 hz.

1

2

3

4 ### *Analysis of eye tracking data*

5 The eye tracking data were converted to screen coordinates. Blinks were removed from the

6 time series based on deviations in pupil area of more than one standard deviation from the

7 mean including 25ms around the blink on- and offsets. After smoothing with a running

8 average kernel of 10 ms and linearly detrending, gaze positions were transformed to

9 velocities expressed as degree visual angle per second. Since gaze velocity profiles differed

10 between translations and rotations during navigation, saccades were detected individually

11 during head rotations and static or translational navigation. During head rotations, saccades

12 were detected using a threshold of 12 times the median-based standard deviation of

13 velocity, during static or translational periods with 6 times the median-based standard

14 deviation of velocity. Saccades shorter than 12 ms were excluded (Engbert & Kliegl, 2003).

15

16 To examine which cues were looked at most during the experiment, we transformed

17 horizontal gaze positions to degrees visual angle and scaled them linearly to match the

18 physical field of view (36 degrees visual angle) to the virtual field of view (85 degrees virtual

19 visual angle). The resulting virtual degrees visual angles were then combined with the virtual

20 head direction to reconstruct the allocentric viewing direction at each point in time. Since all

21 twelve spatial cues were visible exclusively in the upper visual field, we limited our analysis

22 to gaze positions on the upper half of the screen. Moreover, to account for any potential

23 influence of initial viewing angle on this analysis, we excluded all samples recorded before

24 participants rotated at least 90 virtual degrees away from the starting viewing angle (average

25 time excluded at start of experiment: 15.2 seconds). We then computed the intersection

26 between allocentric gaze and a surface at the radius of the extra-maze cues from the centre

27 of the arena for each point in time as follows. We first generated 360 equally spaced vertices

28 at the radius of the extra-maze cues and computing the vectors between the participant's

29 location and all of these vertices. We then selected the respective vertex with the minimal

30 angular distance to the current allocentric viewing direction. This way, we obtained the

31 position of gaze on the arena border or cues at each given point in time. For each vertex we

32 computed the respective viewing time expressed as percent of all samples obtained for each

33 respective participant to account for differences in experiment duration across participants

34 (Figure 3 – figure supplement 2). To examine whether there were differences in viewing

35 times between cues, we then binned vertices into 30 degree bins centred on the cues and

36 compared average viewing time using a repeated-measures ANOVA. However, our specific

37 hypothesis was that especially the cues forming the polarisation axis should be most

1 informative for the task. To test whether these cues were the ones most viewed, we

2 averaged viewing times for the configural landmarks that comprised the polarisation axis (i.e.

3 two pairs of cues of opposite orientation) and compared it to the average of the four cues

4 orthogonal to the polarisation axis using a one-tailed paired t-test.

5

6

7 ***FMRI data pre-processing***

8 Image pre-processing and analysis were performed with the Automatic Analysis Toolbox

9 (https://github.com/rhodricusack/automaticanalysis). This involved using custom scripts

10 combined with core functions from FSL 5.0.4 (http://fsl.fmrib.ox.ac.uk/fsl/) and SPM8

11 (http://www.fil.ion.ucl.ac.uk/spm). SPM was used for an iterative functional image

12 realignment and unwarping procedure to estimate movement parameters (three for rotation,

13 three for translation) and to correct images with respect to gradient-field inhomogeneities

14 caused by motion. To improve co-registration and the creation of a group-specific structural

15 and functional template using the Advanced Neuroimaging Toolbox (ANTS;

16 http://www.picsl.upenn.edu/ANTS/) structural images were de-noised using an optimised

17 non-local means filter (Manjón, Coupé, Martí-Bonmatí, Collins, & Robles, 2010) and mean

18 EPI images were corrected for gradual changes in signal intensity (bias correction) using

19 SPM. Next, structural images were co-registered (based on mutual information) to the

20 functional images using SPM and brain-extraction was performed using FSL. The resulting

21 skull-stripped structural image was segmented into grey matter (GM), white matter (WM)

22 and cerebro-spinal fluid (CSF) voxel masks. Finally, functional images were spatially

23 smoothed with an isotropic 8-mm full-width-half-maximum Gaussian kernel and high-pass

24 filtering with a 128-s cut-off to reduce low-frequency drift.

25

26 ***Physiological artefact correction.***

27 During the 7T-fMRI acquisition of fMRI experiment 1, we recorded the cardiac pulse signal

28 and respiration of participants by means of an MRI compatible pulse oximeter and

29 pneumatic belt (Siemens Healthcare, Erlangen, Germany) at a sampling rate of 50 Hz. In

30 addition, scanner pulses were recorded in an analogue input for synchronisation of fMRI and

31 physiological data at 200 Hz. Due to technical problems, these data were not available for all

32 scanning blocks and participants (average of 2.7 blocks, range 0 to 5 blocks per participant).

33 Physiological artefact correction was performed for fMRI data with available concurrent

34 physiological data. This involved band-pass filtering the pulse data between 20 and 150 bpm

35 (0.3 and 2.5 Hz, respectively) to improve peak detection. Subsequently, RETROICOR was

36 used to create regressors that were fed into the subject-specific fMRI analyses (GLMs) as

37 confound regressors to remove spurious fluctuations. Fluctuations due to cardiac and

1   respiratory phase were each modeled by 6 regressors for sine and cosine Fourier series

2   components extending to the 3rd harmonic. Two additional regressors modeled lower

3   frequency changes in respiration and heart rate with a sliding window analysis following

4   (Hutton et al., 2011).

5

6   ***Region-of-interest (ROI) definition***

7   Based on our a priori hypothesis (Doeller et al., 2010; Kunz et al., 2015), ROI analyses were

8   performed for the right entorhinal cortex (EC). Right EC ROIs were created on the Montreal

9   Neurological Institute (MNI152) T1 template using a probabilistic atlas based on

10   cytoarchitectonic mapping of ten human post-mortem brains (Amunts et al., 2005) with FSL

11   5.0.4 (http://fsl.fmrib.ox.ac.uk/fsl/). The probability threshold was conservative (95%) for the

12   estimation of hexadirectional orientations and liberal (0%, i.e. including all voxels with non-

13   zero probability) for the small volume correction of the mask. Thresholded masks were

14   binarised and converted to NiFTI file format and then normalised to the space of the

15   individual functional images via the group-specific EPI template (Figure 4 – figure

16   supplement 1) using the Advanced Neuroimaging Toolbox (ANTS;

17   http://www.picsl.upenn.edu/ANTS/). SPM was used to reslice the ROI mask dimensions to

18   the EPI dimension, which was again followed by binarisation of the masks. Through the

19   same procedure, a right, primary visual cortex (Amunts, Malikovic, Mohlberg, Schormann, &

20   Zilles, 2000) mask (95% threshold) and a mamillary body (Bürgel et al., 2006) mask (25%

21   threshold) were created for control analyses.

22

23   ***Analysis of fMRI time series***

24   Following pre-processing, fMRI time series were modeled with general linear models

25   (GLMs). The different trial phases of the object-location memory task were modeled with two

26   regressors. One regressor was used for the retrieval phase (replacement of an object) and

27   one for the encoding phase (following the location response, when the object was shown at

28   the correct location and could be collected), both of which were associated with a parametric

29   modulator for spatial memory performance to discount large-error trials. Inter-trial-intervals

30   (presentation of a fixation cross on a gray background) were not explicitly modeled and

31   served as an implicit baseline. The presentation of the object cues and the feedback was

32   modeled with two additional regressors. Furthermore, all GLMs included nuisance

33   regressors, comprising at least 6 movement parameters, 2 regressors for signal fluctuations

34   across white and gray matter voxels and 1 regressor to model time points with frame-wise

35   displacements (Power, Barnes, Snyder, Schlaggar, & Petersen, 2012) larger than 0.5 mm.

36   In addition, physiological signals have been recorded for a sub-set of participants (see

37   section below for details) which was used to correct for cardiac and respiratory artefacts by

1   means of 14 additional regressors. The main regressors of interest modeled virtual

2   movement periods with two associated parametric modulators (see 'Analysis of

3   hexadirectional activity' below for details). Coefficients for each regressor were estimated for

4   each participant using maximum likelihood estimates to account for serial correlations. All

5   parametric modulators were normalized to have zero mean and thus be orthogonal to the

6   un-modulated regressor. Prior to the second-level random effects analysis, the linear

7   contrast images of the regression coefficients underwent nonlinear normalization to the

8   group-specific template brain using ANTS.

9

10   ***Analysis of hexadirectional activity***

11   The orientation of 6-fold rotational symmetry of entorhinal activity (referred to as

12   'hexadirectional activity' and consistent with grid-cell representations in humans [10]) was

13   estimated in participant's right EC using a quadrature-filter approach on fMRI data during

14   fast movements in all trial phases [4,5]. Participant's virtual-navigation fMRI data entered a

15   general linear model (GLM) with two parametric modulators of a movement regressor.

16   These modelled the sine and cosine of running direction $\theta(t)$ in periods of 60° (i.e. $\sin(6*\theta(t))$

17   and $\cos(6*\theta(t))$) for participant's 50% fastest movement time points, where grid-cell-like

18   representations can be reliably detected (Doeller et al., 2010; Kunz et al., 2015).

19   Multiplication by 6 transformed running direction into 60° periodic space to create regressors

20   sensitive to activation showing a six-fold rotational symmetry in running direction. Activations

21   with six evenly spaced peaks as a function of running direction will produce parameter

22   estimates β_1 and β_2 for the two regressors with large amplitude $\sqrt{(\beta_1^2 + \beta_2^2)}$. To this end,

23   running direction $\theta(t)$ was arbitrarily aligned to 0° of the coordinate system underlying the

24   virtual reality engine. Participants were not aware of the environmental coordinate system.

25   The relationship between the underlying coordinate system and the polarisation axes

26   (defined by extra-maze cues) differed between fMRI experiment 1 and fMRI experiment 2.

27   The orientation of the polarisation axis (i.e. 0°) had an angular offset from the underlying

28   coordinate system of 15° in fMRI experiment 1 and 90° in fMRI experiment 2. This made it

29   unlikely that an anchoring of grid-cell representations to polarisation axes were due to other

30   factors, such as viewing direction during the start of the experiment, which was -15° in fMRI

31   experiment 1 and -90° in fMRI experiment 2, relative to the visible polarisation axes. Next,

32   the parameter estimates of the two parametric modulators (β_1 and β_2) were extracted from

33   the right EC ROI and used to calculate preferred orientation in 60° space (varying between

34   0° and 59°). A participant's mean orientation of hexadirectional activity was defined as $\varphi_{60°} =$

35    $\arctan(\beta_1/\beta_2)$, where β_1 is the averaged beta value for $\sin[6*\theta(t)]$ and β_2 is the averaged beta

36   value for $\cos[6*\theta(t)]$ across voxels of the right EC. Dividing by six transformed the mean

1 orientation $\varphi_{60°}$ back into standard circular space of 360° for one of the three putative grid

2 axes (the remaining two being 60° and 120° relative to the first).

3

4 Our main research question was if environmental geometry affects the orientation of putative

5 grid-cell representations (see below for a description of the statistical test procedure). To

6 additionally cross-validate effects of entorhinal hexadirectional activity (Bellmund et al.,

7 2016; Doeller et al., 2010; Kunz et al., 2015), we tested the temporal stability of preferred

8 orientations and their regional specificity in a split-half procedure (Experiment 1). This was

9 done only for experiment 1, because data acquisition was roughly twice as long and SNR

10 likely higher due to high-field scanning compared to experiment 2, which warranted a

11 sacrifice in sensitivity for the main research question.

12 The procedure involved testing activation differences in the second half of the data with six-

13 fold rotational symmetry that was aligned with the (potentially environmentally determined)

14 hexadirectional activity estimated from the first half of the data. More specifically, the second

15 GLM contained regressors for both 'aligned' and 'misaligned' runs relative to the estimated

16 hexadirectional activity (respectively, this means running directions were either less than ±

17 15° or more than ± 15° oriented relative to the nearest axis of hexadirectional activity). As for

18 the estimation procedure, regressors modeling six-fold rotational symmetry captured

19 participant's 50% fastest movement time points. Participants' contrast values (aligned >

20 misaligned) then entered a second level random-effects analysis to test for hexadirectional

21 activity in the entire brain volume acquired. Significant activation in the right EC would

22 indicate temporal stability and regional specificity of putative grid orientation.

23 Having evaluated temporal stability and regional specificity of the quadrature-filter approach

24 for investigation of grid-cell-like representations in fMRI experiment 1, we decided to

25 maximise statistical power addressing the main research question of environmental effects

26 on hexadirectional activity in fMRI experiment 2.

27

28 ***Analysis of environmental anchoring of hexadirectional activity***

29 We tested environmental anchoring of the hexadirectional activity relative to the polarisation

30 axes by using a V test for circular homogeneity (Berens, 2009). The V test for circular

31 homogeneity is similar to the Rayleigh test for circular homogeneity and can be used if an a-

32 priori hypothesis of a certain mean direction in a sample of angles is being tested. Due to

33 our hypothesis of a relationship between the orientation of the grid-system and anisotropy in

34 spatial information derived from angular changes to polarising cues, we tested participant's

35 putative grid orientations in 0°-60° space (Figure 4B and Figure 6A) for the presence of a

36 mean direction aligned 30° off the polarisation axis.

37

1 **Author contributions:**

7

8 **Acknowledgements**

22

23

24

25 **Figures:**

26

1 **Figure 1. Spatial information is anisotropic and affects optimal self-localisation using**

2 **grid cells. A** Spatial information during movement in polarised environments is anisotropic.

3 Left: schematic of arena with radius R, and polarising cues at distance L. Right: three

4 example paths in different directions and through the centre are shown (black arrows at

5 angle θ; Path lengths are equal to distance of the cue to the centre). The change in cue

6 direction from the observer's heading (δσ) is maximal on paths perpendicular to the

7 polarisation axis (note: this is also the case on average if paths are not centred on the

8 middle, but distributed evenly throughout the environment). **B-D** We simulated decoding of

9 position estimates from the activity of grid cell ensembles with patterns oriented at different

10 angles relative to the axis of lowest spatial certainty. Uncertainty in spatial information was

11 introduced by adding Gaussian errors to the position information input to the grid cells.

12 These errors were generated independently for each module of grid cells. Anisotropy was

13 created by separately varying the standard deviations of the error in two orthogonal axes. **B**

14 illustrates an example: the subject's actual location is at the origin; red shading indicates a

15 two-dimensional probability density distribution for error generation, with different standard

16 deviations in each axis; and crosses indicate four independently generated noisy position

17 estimates, drawn from this distribution and be input to each of the grid cell system's four

18 modules. **C** Schematic illustration of two grid orientations either aligned with the uncertainty

19 axis (left panel, arrows indicate hexadirectional orientations associated with a grid), or

20 rotated 30° (right panel). The number of depicted grid fields differ only for illustration

21 purpose. **D** Position decoding error, defined as the mean maximum-likelihood estimate

22 square error (MMLE; cm^2), was largest when one grid axis was aligned at 0° (as shown in

23 panel B, left side). Solid black: errors with s.d. 5cm and 0cm; dashed grey line: 5cm and

24 1.67cm. Grid orientation is defined as the minimal angular offset of a grid axis from the axis

25 of greater uncertainty (this is analogous to hexadirectional offset of entorhinal fMRI activity

26 described below). Error bars indicate 95% confidence interval (n=150,000).

27

28
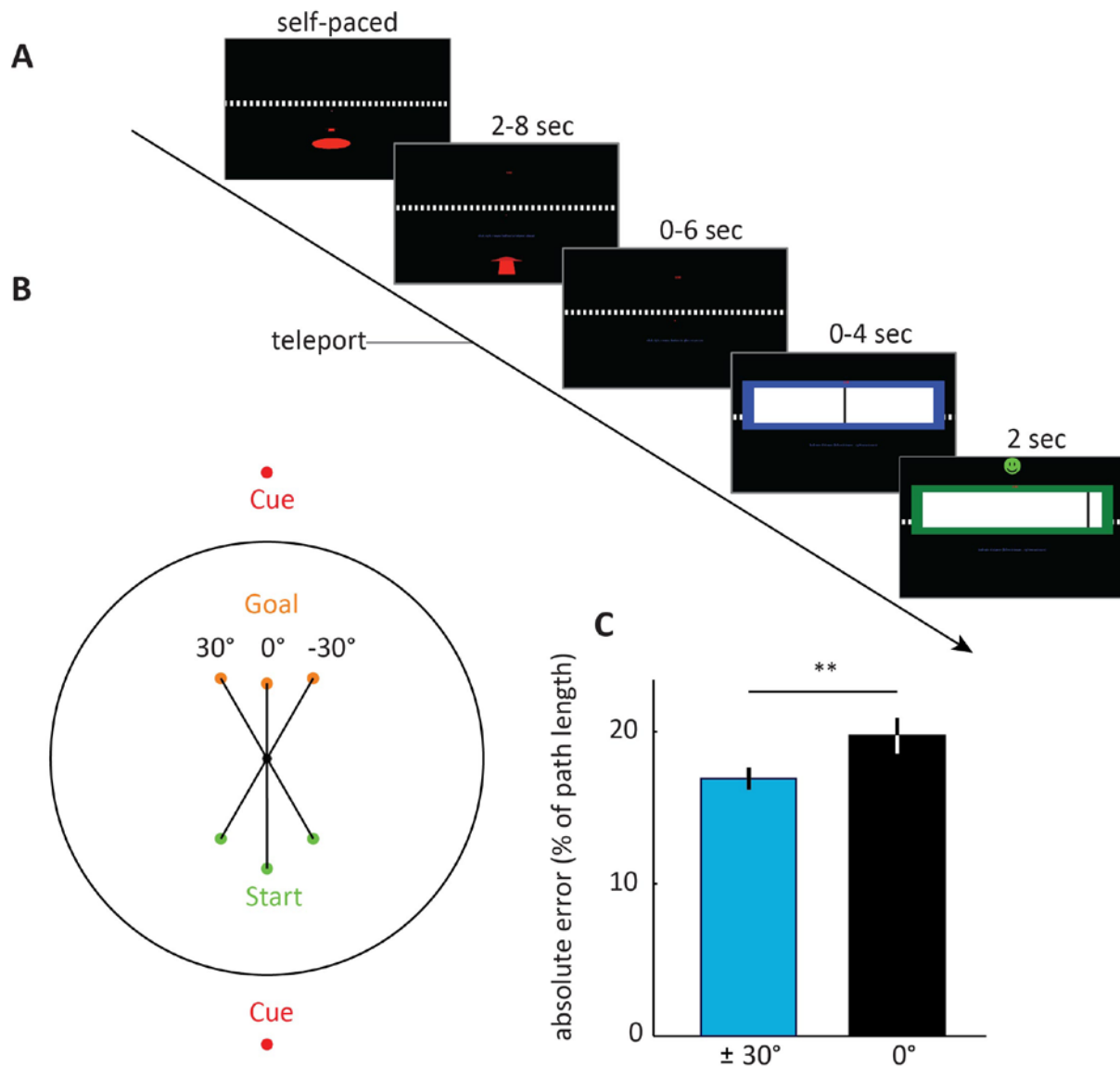
Figure 2. Distance estimation is most accurate on oblique paths. A Trial event sequence. Following a familiarisation phase, participants navigated to a start location (indicated by the red circle and arrow) and initiated teleportation in a given direction, either along a polarisation axis or at ±30° offset, see B and Figure 2– figure supplement 1. Teleportation distance was experimentally manipulated and participants gave a distance estimate at the goal location by sliding a response bar (black slider in blue box). The cue was visible both at the start and the goal location (small red dot at eye height, in this example trial shown at the direction the arrow is pointing). Subsequently, participants received feedback. **B** Schematic of the three possible path angles shown at the same distance. Path distance varied from trial to trial (see Materials and Methods). Note that no boundary was present. The black circle only illustrates an analogy to the arena environments used in the fMRI experiments. Start and goal positions are illustrated by green

1 and orange dots, respectively. **C** Distance estimation was most accurate on oblique paths,

2 consistent with anisotropy of spatial information. Error bars show S.E.M. over participants.

3
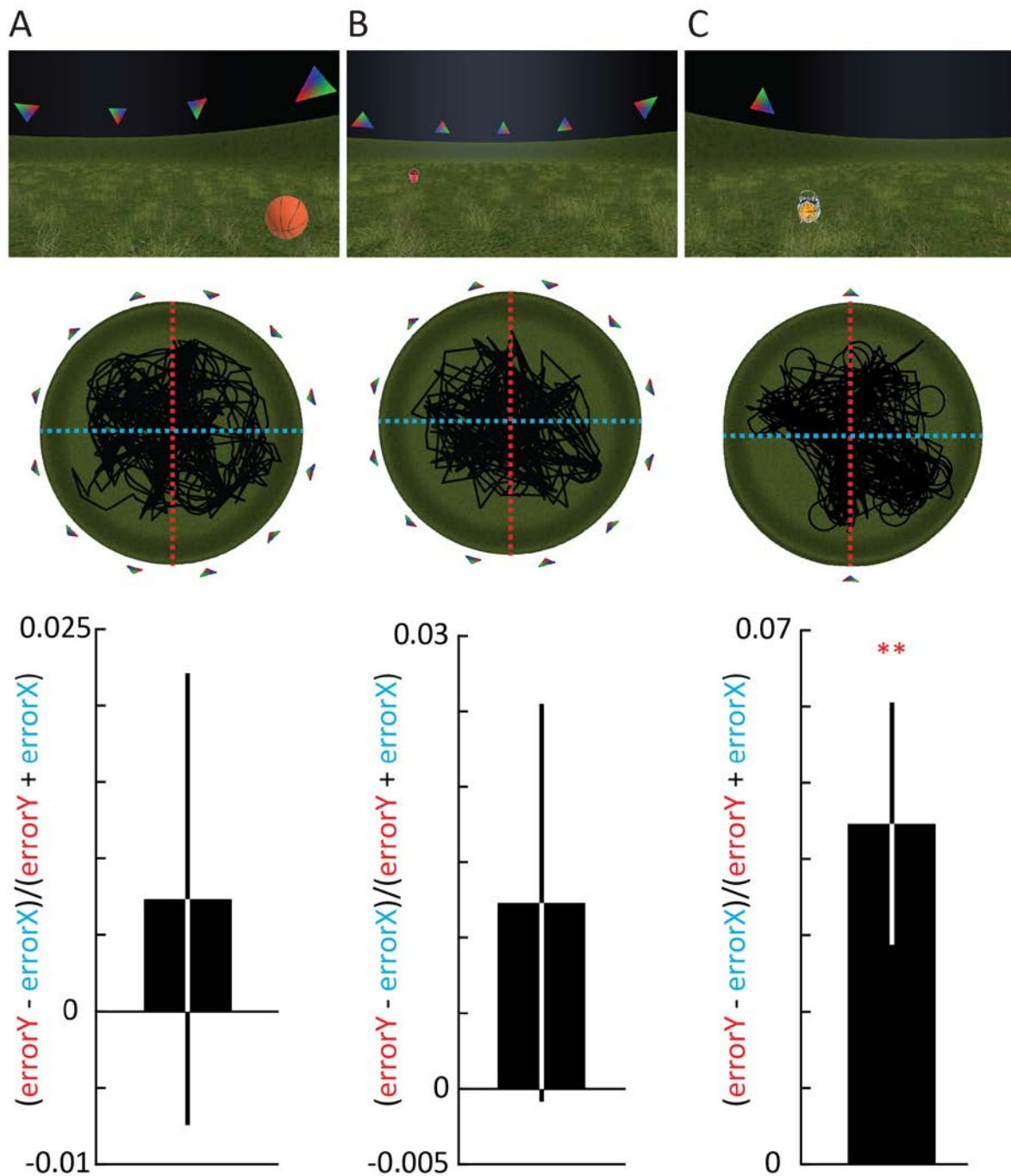
4

5 **Figure 3. Spatial memory performance is anisotropic. Top** First person view of the

6 virtual environments used in **A** fMRI experiment 1, **B** the eye tracking experiment, and **C**

7 fMRI experiment 2. **Middle** aerial view. . Human participants performed a free-navigation,

8 object-location memory task (one example object shown on grassy plane, see Materials and

9 Methods). In fMRI experiment 1 and the eye tracking experiment, an implicit polarisation axis

10 was defined through the configuration of cues, i.e. the switch between upright and downward

1   triangles. In fMRI experiment 2, an explicit polarisation axis was defined with two triangular

2   cues alone. Black lines in aerial view show the paths of exemplary participants. Red dashed

3   line indicates the polarisation axis (Y dimension), whereas the cyan dashed line indicates

4   the orthogonal X dimension.**Bottom** Bars show the anisotropy in spatial memory error.To

5   avoid potential bias, we matched the number of trials in which participants faced (or moved)

6   parallel and perpendicular to the polarisation axis (±45°). This measure yields positive

7   values if the error on the Y dimension (i.e. the polarisation axis) are larger than on the X

8   dimension. This anisotropy in spatial memory performance in the environment with only two

9   polarising cues corroborates the theoretical predictions of an anisotropy in spatial

10   information (Equation 1, Figure 1 and Figure 1 – figure supplement 1). Error bars show

11   S.E.M. over participants.

12
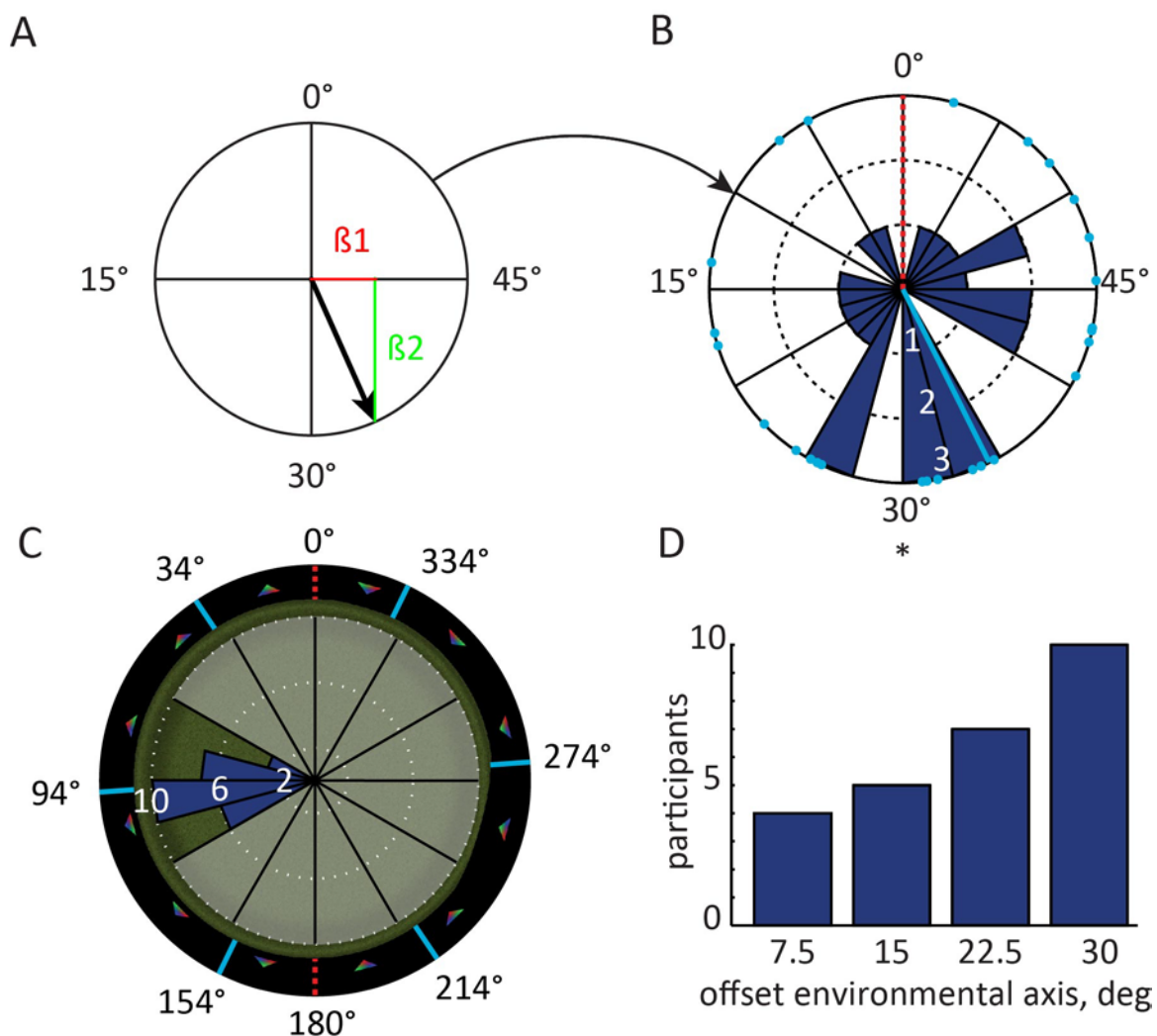
13

14   **Figure 4. Hexadirectional activity in entorhinal cortex aligns perpendicular to the**

15   **polarisation axis. A** Analysis procedure: the preferred orientation of hexadirectional fMRI

16   activity in the entorhinal cortex was estimated by first fitting a general linear model (GLM) to

1   the data with 60°-periodic sine and cosine regressors. This yields the associated parameter

2   estimates ß1 and ß2, respectively. The preferred orientation in 60°-space (black arrow) can

3   be derived from ß1 and ß2 (see Materials and Methods). The corresponding preferred

4   orientation of hexadirectional activity in 360°-space can then be deduced. Here, this

5   corresponds to multiples of 60° centered on 34° (light blue lines in C) relative to the

6   polarisation axis (red dashed line) at 0°. **B** Individual, preferred orientations in 60°-space

7   (light blue dots) in right entorhinal cortex clustered at roughly 30° offset relative to the

8   polarisation axis; mean orientation = 34° (light blue line). **C** Histogram of preferred

9   hexadirectional activity plotted in full circular space (360°). Note that one of the

10   hexadirectional axes is roughly orthogonal to the polarisation axis, in line with optimal angles

11   for self-localisation (Figure 1D) **D** Absolute angle between nearest axis of hexadirectional

12   activity shown in B and the polarisation axis illustrate a tendency towards maximal

13   misalignment. Note that the maximum offset is 30° due to the 60° periodicity of

14   hexadirectional activity.
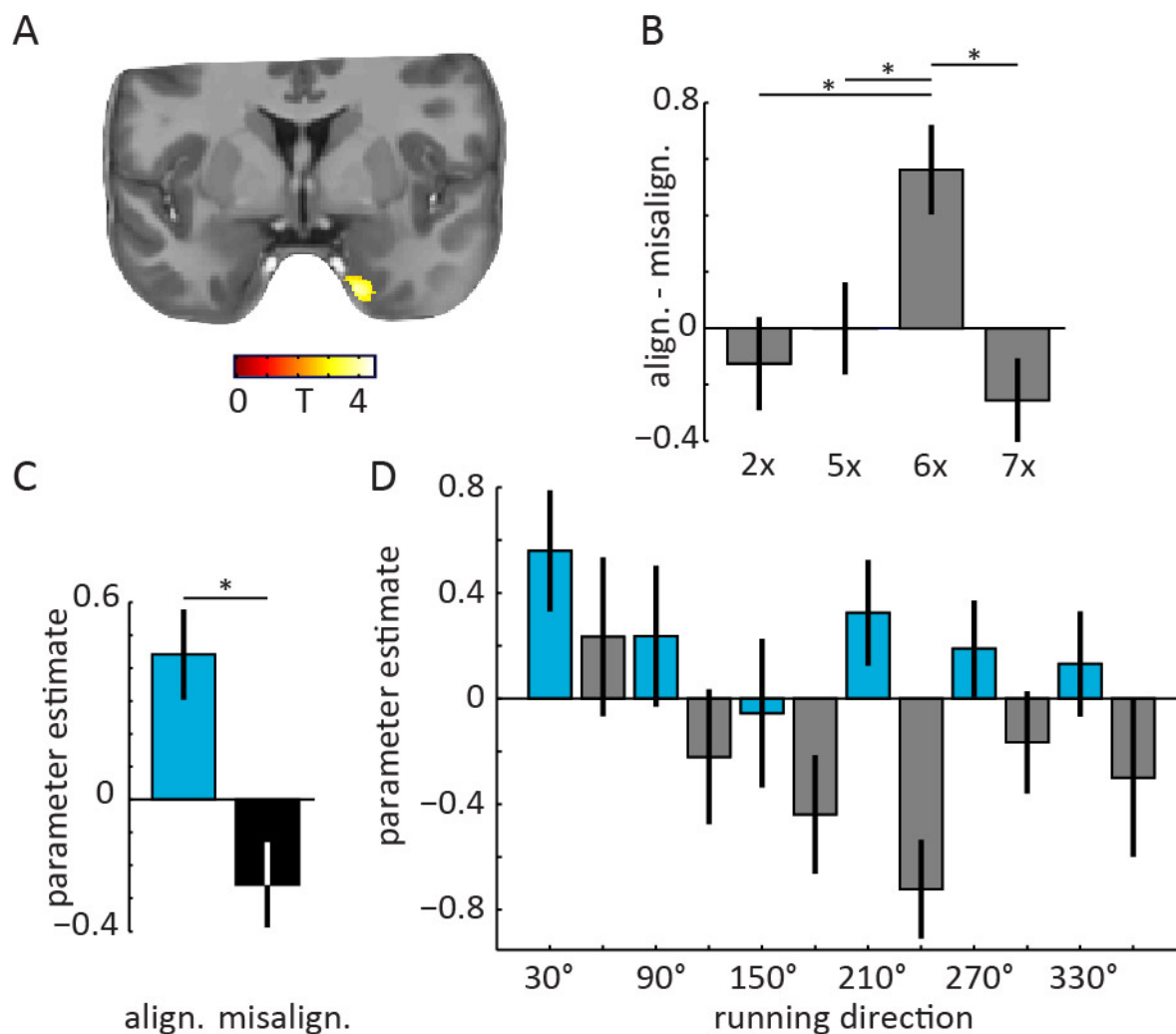
15   **Figure 5. Cross-validation of hexadirectional activity in entorhinal cortex and control**

16   **models. A** A whole-brain cross-validation confirmed that entorhinal activity was increased

1   on runs aligned with the predicted grid (i.e. runs in 30°-wide bins centered on 30°, 90°, 150°

2   etc. indicated by light blue arrows in C and D; see Materials and Methods for details). Image

3   is thresholded at p<0.001 uncorrected for display purpose. Effects are significant at T(25) =

4   4.44, small-volume FWE-corrected p=0.034. The T statistic (colour bar) is overlaid on the

5   structural template. Across the cerebrum no other peaks were observed at p<0.001,

6   uncorrected. **B** In agreement with grid-cell-like representations, runs aligned versus

7   misaligned show largest activity increase for 6-fold (6x) rotational symmetry but not for

8   biologically implausible control models. Next to 5- and 7-fold rotational symmetry, 2-fold

9   symmetry was tested to rule out a direct effect of running parallel to the polarisation axis or

10   not. For all analyses the aligned condition was centered at an angle equivalent to 90° from

11   the polarisation axis (e.g. 30° for 6-fold symmetry). **C** Parameter estimates of runs aligned

12   (light blue, see schematic grid in Figure 1C right panel) and misaligned (black) with the

13   predicted hexadirectional orientation extracted from the peak voxel in A. **D** To examine the

14   influence of different running directions, we plotted the parameter estimates for separate

15   regressors of 12 directional across the entire time-series of fMRI data from the peak-voxel in

16   A. Note the alternating pattern of activity aligned and misaligned. Bars show means and S.

17   E. M. across participants.

18
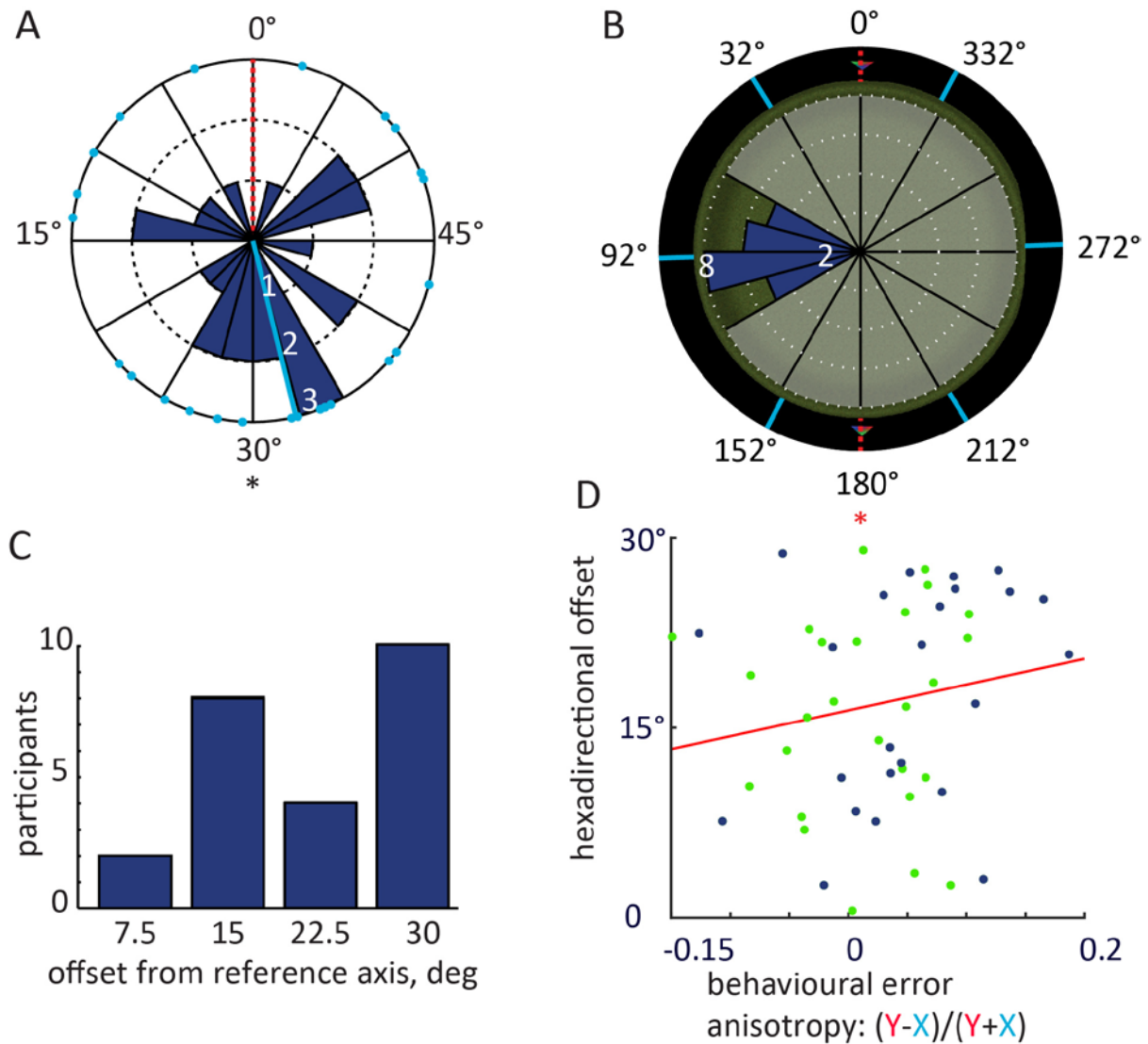
1

2 **Figure 6. Environmental effects on hexadirectional activity in experiment 2 and**

3 **correlation with behaviour. A** Preferred hexadirectional activity in 60°-space (light blue

4 dots) in right entorhinal cortex clustered at roughly 30° offset relative to the polarisation axis

5 (mean orientation = 32.28°; light blue line), in line with optimal angles for self-localisation

6 (Figure 1D) **B** Histogram of preferred hexadirectional orientations plotted in full circular

7 space (360°) onto a top-down view of the arena. Note that one of the putative grid axes is

8 roughly orthogonal to the polarisation axis. **C** Absolute angle between nearest axis of

9 hexadirectional activity shown in B and the polarisation axis. Note that the maximum offset is

10 30° due to the 60° periodicity of hexadirectional activity. **D** Hexadirectional offset correlates

11 with anisotropy in spatial memory performance across participants. The positive relationship

12 indicates that participants with a more orthogonal orientation of hexadirectional activity were

13 relatively more precise in placing objects on the X dimension than the Y dimension. Green

14 dots: participants from fMRI experiment 1. Blue dots: participants from fMRI experiment 2.
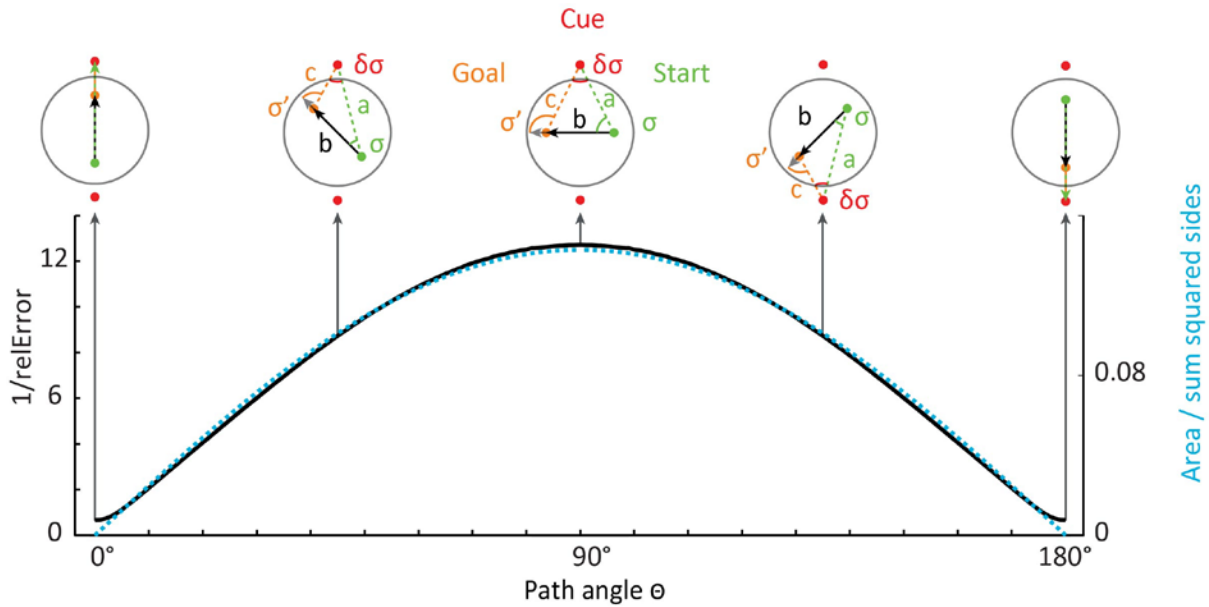
15

1   **SUPPLEMENTAL INFORMATION**

2

3   **Supplemental Figures:**

4

5

6
7   **Figure 1 – figure supplement 1. Triangulation under noise in circular and square**

8   **environments.** To test the impact of anisotropic optic flow information on spatial

9   computations, we performed a biologically inspired simulation of Euclidean triangulation. For

10   example, an estimate of the distance between start and end points was computed from

11   noisy estimates of the angles and distance to one of the cues using equation 2. All sides (a-

12   c) of a triangle served as both inputs and distance to be estimated, before the results were

13   averaged on one iteration. The median noise resilience (1/relative error [relError]) across

14   iterations is plotted in black. On a given iteration, relErr is determined as the absolute

15   distance error / side length, averaged across the three sides of each triangle. Black arrows

16   indicate example paths between two observer positions (start in green and goal in orange,

17   always crossing the centre; see Materials and Methods for details). Red dots show

18   polarising cues. Most precise triangulation was achieved on paths orthogonal to the

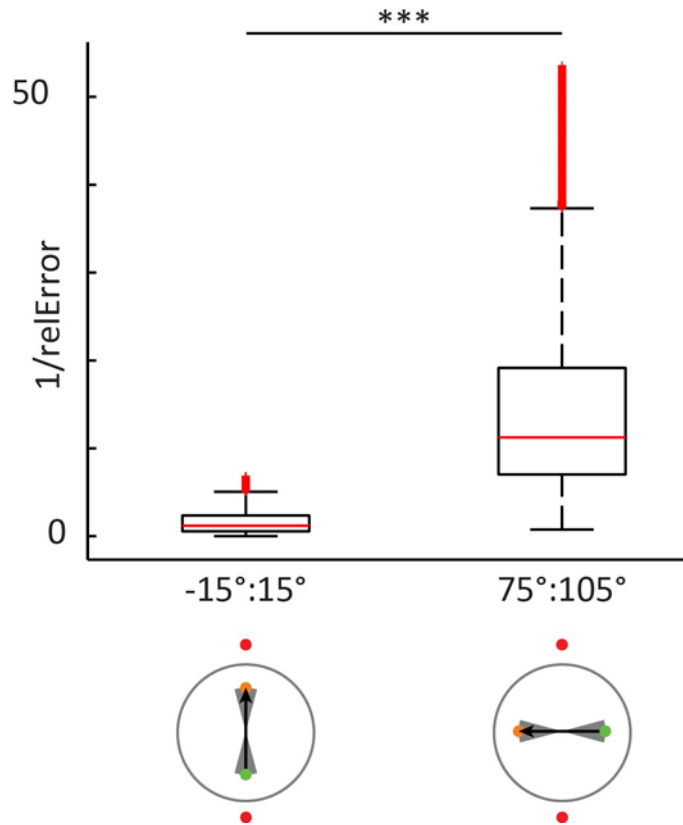19   polarisation axis ($10*10^3$ repetitions for each triangle, 90° ±15° versus 0° ±15°, two-sided

20   Wilcoxon signed-rank test: Z=1026.42, p<0.001). Optimal path angle was well predicted by a

21   quality measure for triangulation (triangle area / sum of squares of the side lengths; R=0.99,

22   p<0.001). This measure increases for more equilateral triangles.

23
24

1

2

3 **Figure 1 – figure supplement 2. Magnitude of noise resilience of directional bin of**

4 **paths centered on peaks and troughs of Figure S1**. The most accurate triangulation was

5 achieved on paths orthogonal to the polarisation axis. $10*10^3$ repetitions for each triangle,

6 90° ±15° versus 0° ± 15°, two-sided Wilcoxon signed-rank test: Z=1026.42, p<0.001. The

7 gray shaded area in the bottom panels indicate the range of paths that were tested. The box

8 edges denote the 25th and 75th percentiles and central red mark the median. The whiskers

9 extend maximally to $q_3 + 1.5 * (q_3 − q_1)$ and minimally to $q_1 − 1.5 * (q_3 − q_1)$, where q_1 and q_3

10 are the 25th and 75th percentiles, respectively. A red + denotes points outside this range,

11 with the exception of the upper 10% of values that were omitted for display purposes.
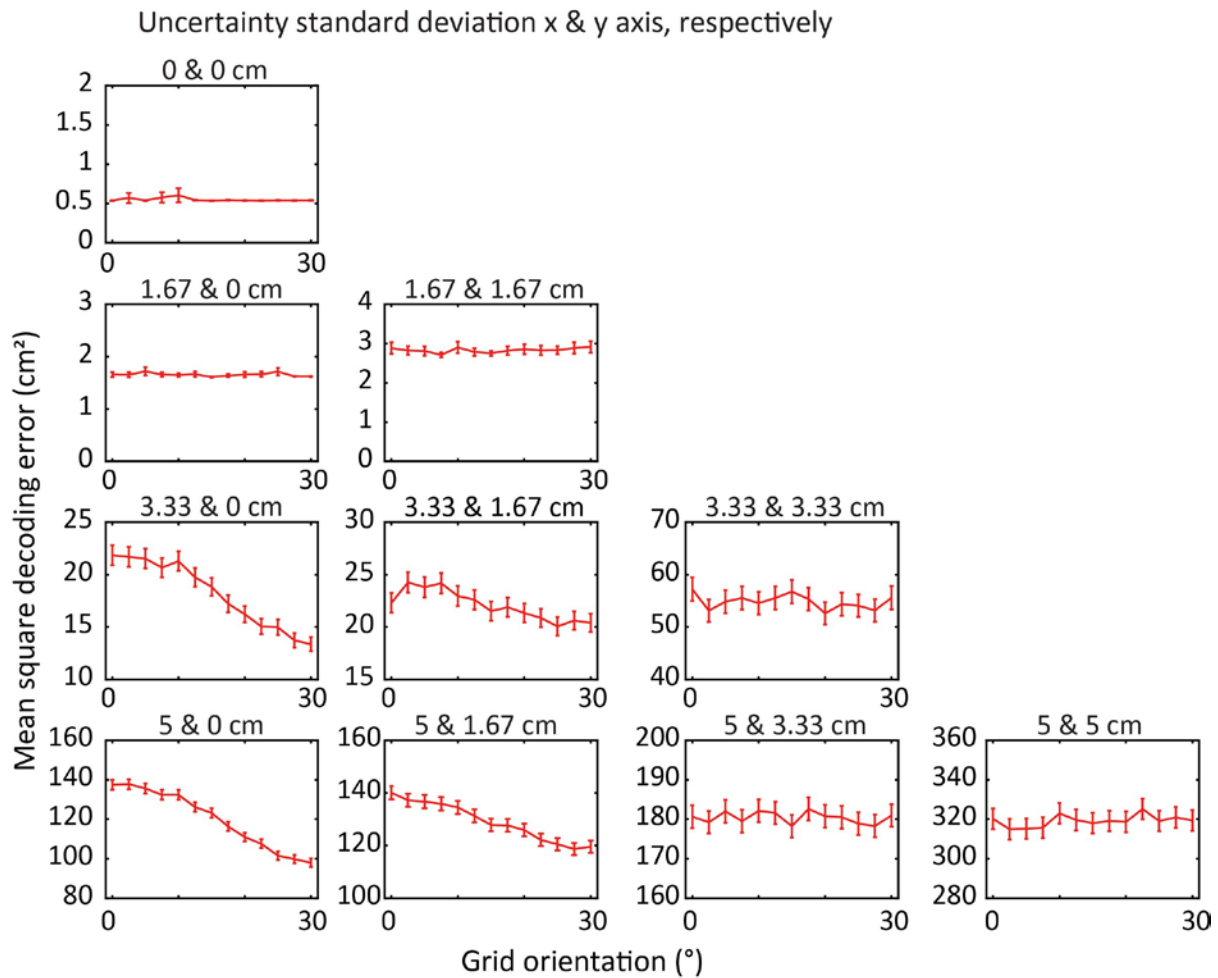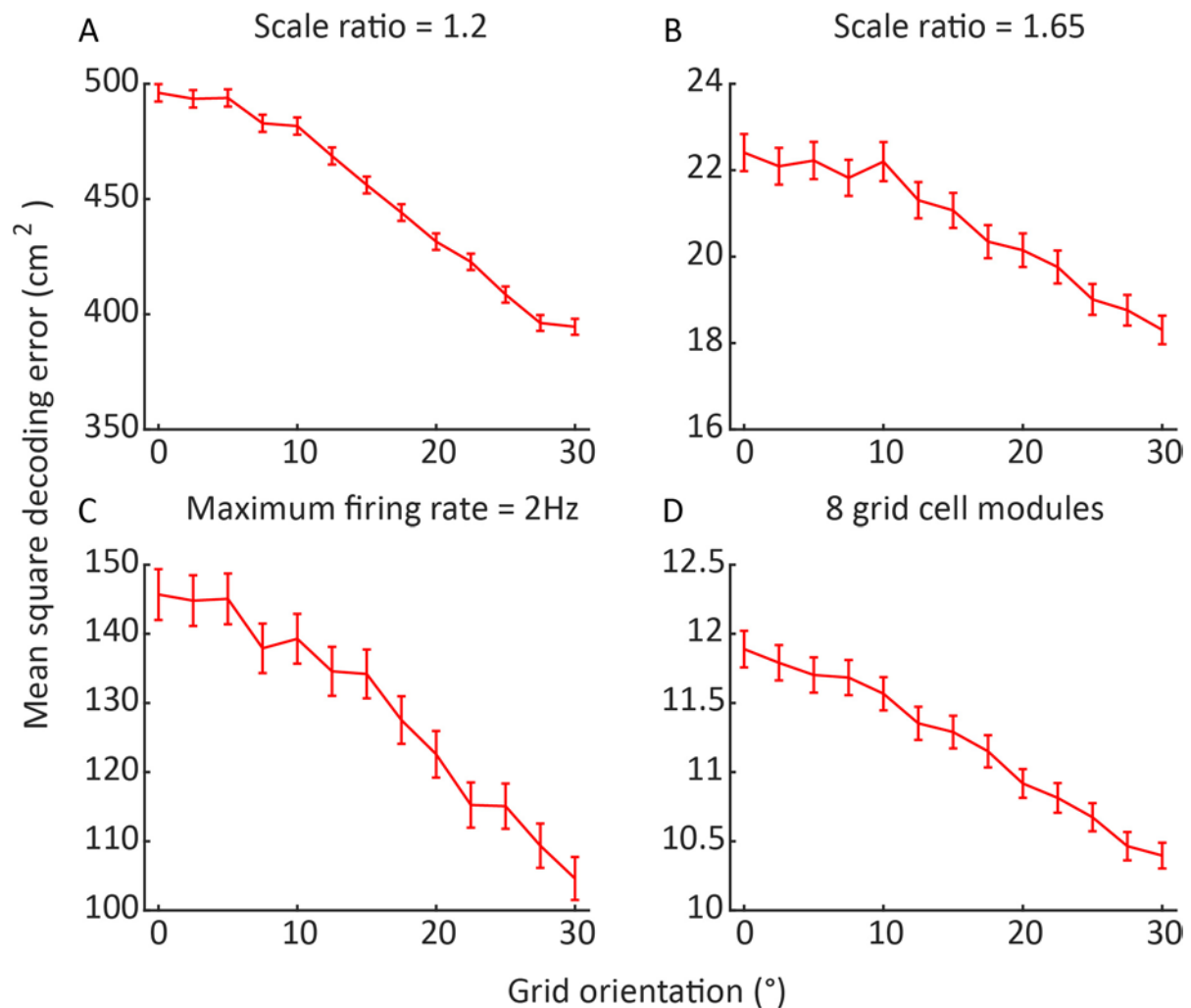
12 Statistical testing included all data.

13
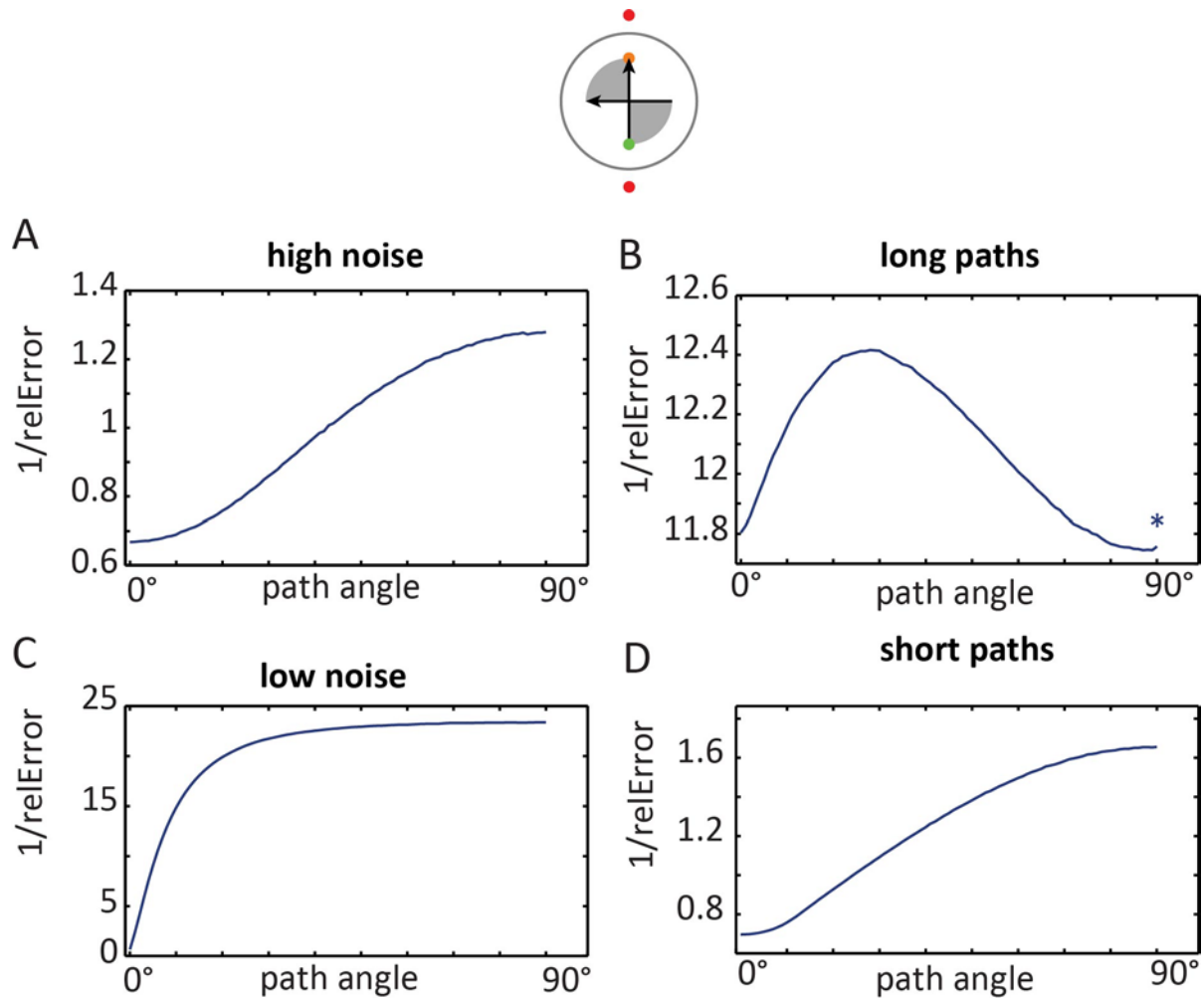
Figure 1 – figure supplement 3. Effects of noise levels and path length on optimal triangulation paths Environment with a single axis are defined by two cues (analogous to the two fMRI experiments and the behavioural experiment). All (A, C, D) except the long path condition (B) yielded an optimum at 90°. However, this extreme case never occurred for participant's paths in the fMRI experiments due to the limitations of the circular boundary. The average length of straight (+-45°) paths was 11% of the polarisation axis' length in fMRI experiment 1 (12% in fMRI experiment 2) – See Figure S6E-F. High noise = randomly sampled from a distribution with a 10 times larger sigma (62.6, instead of 6.26, see Materials and Methods). Low noise = randomly sampled from a distribution with a 10 times smaller sigma (0.626, instead of 6.26). Long paths = simulated path length was equal to the length of the polarisation axis (instead of 50%, see Materials and Methods). Short paths = simulated path length was 5% of the length of the polarisation axis (instead of 50%, see Materials and Methods). Asterix = plots have been smoothed with a 5°-wide kernel for display purposes. The gray shaded area in the top panels indicates the range of paths that were used.

1

2

Figure 1 – figure supplement 4. More extreme anisotropy in spatial uncertainty results in a more pronounced dependency of self-localisation accuracy on grid orientation.

The performance of grid cell systems was assessed while independently varying the degrees of spatial uncertainty in two orthogonal axes. When uncertainty is equal in both axes performance does not depend on the orientation of the grid pattern. As uncertainty becomes more anisotropic, self-localisation is more accurate in grid cell systems in which the grid pattern axes are aligned away from the axis of greatest spatial uncertainty.

1

Figure 1 – figure supplement 5. The dependency of self-localisation accuracy on grid

**orientation is stable within reasonable sets of grid cell system parameters.**

Performance is consistently best when the grid axes are aligned away from the axis of least

spatial uncertainty, across variations in the parameters of the grid cell system. Error bars

indicate 95% confidence interval, n = 150,000 unless otherwise specified. **A** Grid period

scaling factor reduced to 1.2. **B** Grid period scaling factor increased to 1.65**. C** Grid cell

maximum firing rate reduced to 2Hz. (In order to compensate for increased effects of noise

in this system, the number of cells per module was quadrupled. Due to the high

computational intensity of this simulation n = 75,000.) **D** Four further grid cell modules

added, with scales continuing to increase geometrically.

12
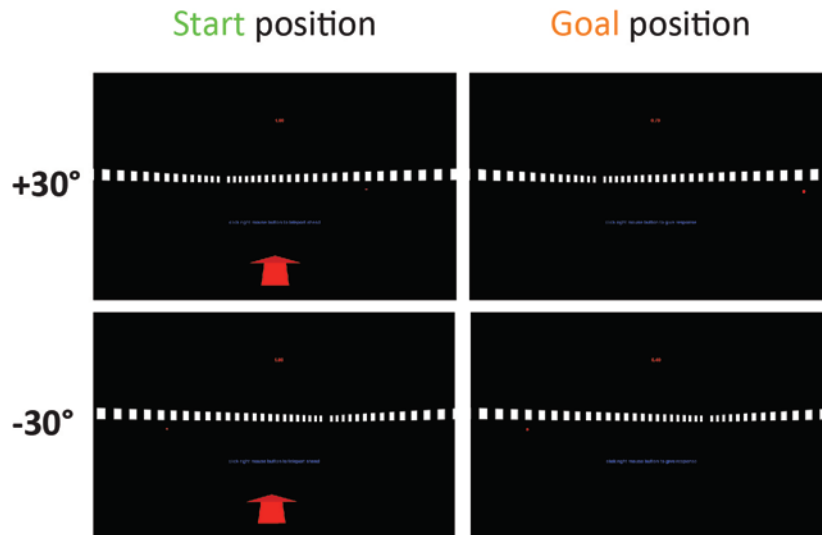
1
2
3 **Figure 2 – figure supplement 1. Additional views of the behavioural experiment at the**

4 **beginning (Start) and end (Goal) of a path.** Note that the background was rendered at

5 infinity (see Materials and Methods), such that it did not change during translations in the

6 ±30° or the 0° condition (Figure 2BC).

7
8

1
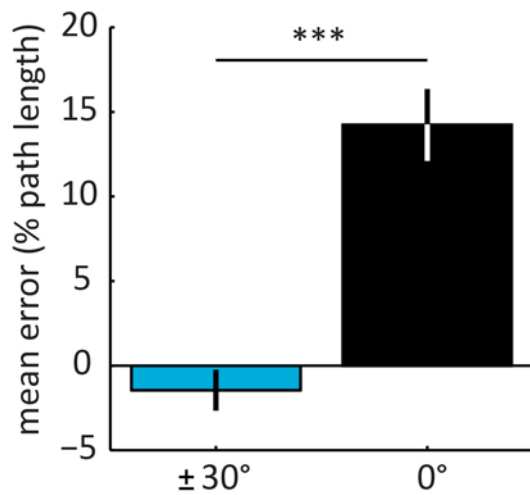
2
3
4 **Figure 2 – figure supplement 2. Accuracy (mean estimation error in percent of correct**

5 **path length) in the behavioural experiment** (Figure 2). Paths along the polarisation axis

6 (0°) yielded less accurate distance estimation than oblique paths (±30°). Paired, two-sided t-

7 test N=20; T(19) = 5.47, p<0.001. See Figure 2C for an effect in the same direction for

8 precision (absolute error). Bars show errors in percent of correct path length averaged

9 across participants +- S. E. M.; Mean 0° condition = 11.8 %; Mean ±30° condition= -0.8 %.

10
11
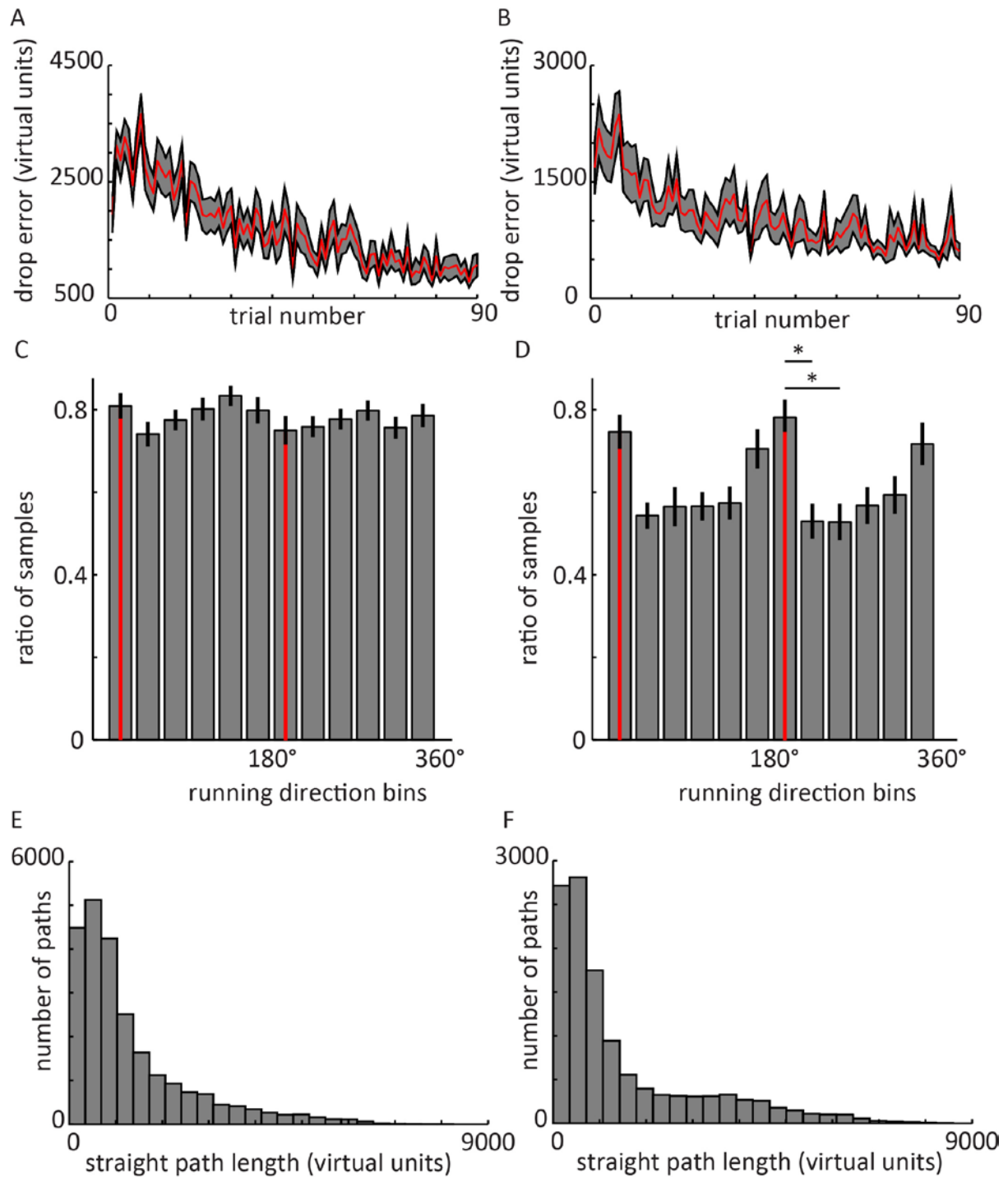
1
2
3
4 **Figure 3 – figure supplement 1. Behavioural analyses of fMRI experiment 1 (A, C, E)**
5 **and fMRI Experiment 2 (B, D, F).** Spatial memory performance: the decreases in drop error
6 indicate that participants in both experiments were able to successfully navigate and
7 remember locations in the sparse virtual environments. Participants learned the locations of
8 6 objects in fMRI experiment 1 (A) and 4 objects in fMRI experiment 2 (B; See Materials and
9 Methods). Red line denotes mean drop error (i.e. Euclidean distance in virtual units between

1   participants' response location and the correct location of a given object on a given trial)

2   across participants. Gray outline denotes standard error of the mean. For display purposes,

3   results are shown up to trial number 90 for consistency. Variations in the number of trials

4   across participants were due to differences in self-paced completion of trials. **C-D** Sampling

5   of running directions. The number of samples of movements in 30° bins of running direction

6   was normalised within participants for comparability across participants by dividing it by the

7   maximum number of samples in any of the 12 bins, thereby yielding a maximum value of 1

8   for a bin. **C** FMRI experiment 1 (polarisation axis defined by configural cues), N = 26: A non-

9   parametric Friedman test of median differences among repeated measures of directional

10   sampling was conducted and resulted in a Chi-square value of 9.5, which was not significant

11   (p=0.57). **D** FMRI experiment 2 (polarisation axis defined by non-configural cues), N = 24: A

12   non-parametric Friedman test of median differences among repeated measures was

13   conducted and resulted in a Chi-square value of 36.7, which was significant (p<0.001). Post-

14   Hoc tests with Tukey-Kramer correction for multiple comparisons revealed that particularly

15   runs along the environmental axis at 165° (+-15°) occurred more often than runs oblique at

16   195° (+-15°) and 125° (+-15°). Asterix: p<0.05 Note that both the absence of a difference in

17   fMRI experiment 1, as well as more frequent runs along the polarisation axis in fMRI

18   experiment 2 speak against the possibility that the environmental effects on hexadirectional

19   activity reported above would be due to biases in navigation behaviour. Error bars show

20   S.E.M. over participants. **E-F** Distances of running paths. Histograms show the number of

21   straight paths for different distances. Path length was determined as the Euclidean distance

22   between start and end point of a path with continuous movement and rotations of less than

23   +- 45° (i.e. a 90°-wide bin). FMRI experiment 1 (E): mean = 1316.2 vu. FMRI experiment 2

24   (F): mean = 1493.5 vu.

25

26

27

28

29

30

31

32

33

34

35

36

37
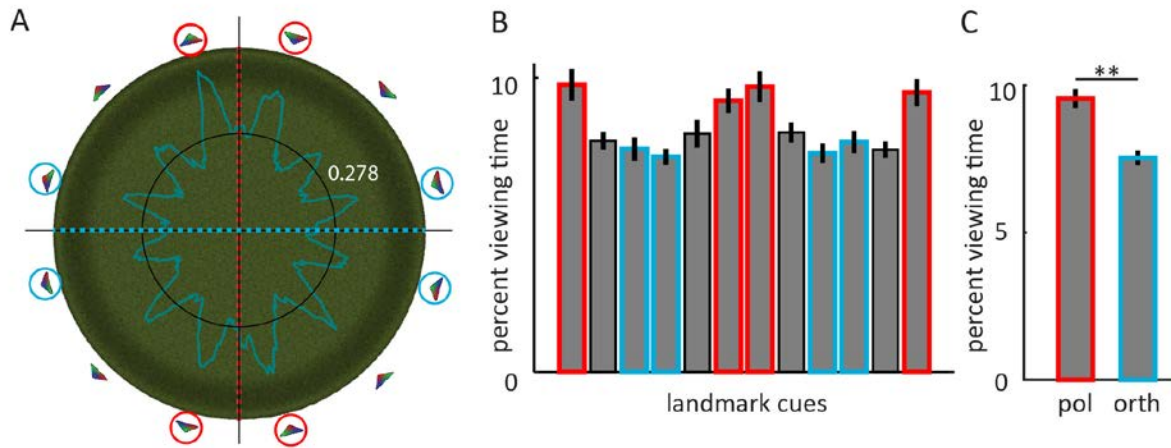
1

2 **Figure 3 – figure supplement 2.** Participant's viewing behaviour in the '12 cue' VR

3 environment (used in fMRI experiment 1 and the eye tracking experiment) reflects stronger

4 reliance on the cues that constitute the polarisation axis. **A** Percent viewing time is plotted

5 for fixations of 360 evenly spaced points on the boundary of the arena defined by the

6 surface of the cues. Black circle: chance level of even distribution of viewing time across all

7 points. Cues marked with red circles constitute the polarisation axis, cues marked with cyan

8 are perpendicular to the polarisation axis. **B** Bars show average percent viewing time in 30°

9 wide bins that were centered on each of the 12 cues. Error bars show S.E.M. over

10 participants. **C** Participants viewed the cues that form the polarisation axis significantly

11 longer than those perpendicular. Error bars show S.E.M. over participants.
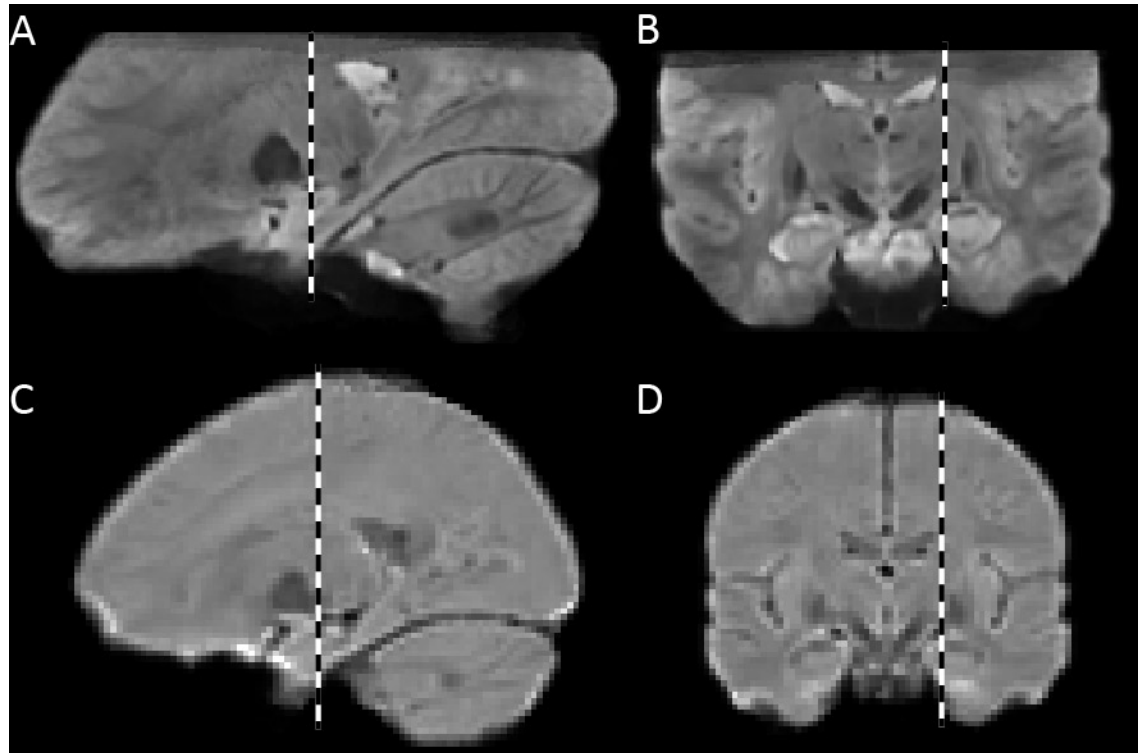
12

Figure 4 – figure supplement 1. Mean functional images across participants used as template brains. **A-B** Template for fMRI experiment 1 (7T scanner). **C-D** Template for fMRI experiment 2 (3T scanner). Dashed lines indicate the location of the slice in the corresponding orientation in the panel above or below. Template images were created with Advanced Neuroimaging Toolbox (ANTS; http://www.picsl.upenn.edu/ANTS/) based on individual, mean 3D echo-planar images. Note the relatively high contrast for functional images in the 7T data, with clear grey and white matter intensity differences even in the medial temporal lobes.

1 **Competing interest:**

2 The authors declare no competing interests.

3

4 **References**

5 Amunts, K., Kedo, O., Kindler, M., Pieperhoff, P., Mohlberg, H., Shah, N. J., Habel, U.,

6 Schneider, F., & Zilles, K. (2005). Cytoarchitectonic mapping of the human amygdala,

7 hippocampal region and entorhinal cortex: intersubject variability and probability maps.

8 *Anatomy and Embryology*, *210*(5–6), 343–352. https://doi.org/10.1007/s00429-005-

9 0025-5

10 Amunts, K., Malikovic, a, Mohlberg, H., Schormann, T., & Zilles, K. (2000). Brodmann's

11 areas 17 and 18 brought into stereotaxic space-where and how variable? *NeuroImage*,

12 *11*(1), 66–84. https://doi.org/10.1006/nimg.1999.0516

13 Bach, D. R., & Dolan, R. J. (2012). Knowing how much you don't know: a neural

14 organization of uncertainty estimates. *Nature Reviews Neuroscience*, *13*(August), 572–

15 586. https://doi.org/10.1038/nrn3289

16 Banino, A., Barry, C., Uria, B., Blundell, C., Lillicrap, T., Mirowski, P., Pritzel, A., Chadwick,

17 M. J., Degris, T., Modayil, J., Wayne, G., Soyer, H., Viola, F., Zhang, B., Goroshin, R.,

18 Rabinowitz, N., Pascanu, R., … Kumaran, D. (2018). Vector-based navigation using

19 grid-like representations in artificial agents. *Nature*, *557*(7705), 429–433.

20 https://doi.org/10.1038/s41586-018-0102-6

21 Bank, R. E., & Smith, R. K. (1997). Mesh Smoothing Using A Posteriori Error Estimates.

22 *SIAM Journal on Numerical Analysis*, *34*, 979–997.

23 https://doi.org/10.1137/S0036142994265292

24 Barry, C., Ginzberg, L. L., O'Keefe, J., & Burgess, N. (2012). Grid cell firing patterns signal

25 environmental novelty by expansion. *Proceedings of the National Academy of*

26 *Sciences*. https://doi.org/10.1073/pnas.1209918109

27 Barry, C., Hayman, R., Burgess, N., & Jeffery, K. J. (2007). Experience-dependent rescaling

28 of entorhinal grids. *Nature Neuroscience*, *10*(6), 682–684.

29 https://doi.org/10.1038/nn1905

30 Barry, C., Heys, J. G., & Hasselmo, M. E. (2012). Possible role of acetylcholine in regulating

31 spatial novelty effects on theta rhythm and grid cells. *Frontiers in Neural Circuits*,

32 *6*(February), 1–13. https://doi.org/10.3389/fncir.2012.00005

33 Bellmund, J. L. S., Deuker, L., Navarro Schröder, T., & Doeller, C. F. (2016). Grid-cell

34 representations in mental simulation. *ELife*, 1–21. https://doi.org/10.7554/eLife.17089

35 Berens, P. (2009). CircStat: A MATLAB toolbox for circular statistics. *Journal of Statistical*

36 *Software*, *31*(10), 1–21. https://doi.org/10.1002/wics.10

37 Burak, Y., & Fiete, I. R. (2009). Accurate Path Integration in Continuous Attractor Network

Models of Grid Cells. *PLoS Computational Biology*, *5*(2), e1000291. https://doi.org/10.1371/journal.pcbi.1000291

Bürgel, U., Amunts, K., Hoemke, L., Mohlberg, H., Gilsbach, J. M., & Zilles, K. (2006). White matter fiber tracts of the human brain: Three-dimensional mapping at microscopic resolution, topography and intersubject variability. *NeuroImage*, *29*(4), 1092–1105. https://doi.org/10.1016/j.neuroimage.2005.08.040

Burgess, C. P., & Burgess, N. (2014). Controlling Phase Noise in Oscillatory Interference Models of Grid Cell Firing. *Journal of Neuroscience*, *34*(18), 6224–6232. https://doi.org/10.1523/JNEUROSCI.2540-12.2014

Burgess, N. (2006). Spatial memory: how egocentric and allocentric combine. *Trends in Cognitive Sciences*, *10*(12), 551–557. https://doi.org/10.1016/j.tics.2006.10.005

Burgess, N., Barry, C., & O'Keefe, J. (2007). An oscillatory interference model of grid cell firing. *Hippocampus*, *17*(9), 801–812. https://doi.org/10.1002/hipo.20327

Bush, D., Barry, C., & Burgess, N. (2014). What do grid cells contribute to place cell firing ? *Trends in Neurosciences*, 1–10. https://doi.org/10.1016/j.tins.2013.12.003

Bush, D., Barry, C., Manson, D., & Burgess, N. (2015). Using Grid Cells for Navigation. *Neuron*, *87*(3), 507–520. https://doi.org/10.1016/j.neuron.2015.07.006

Carpenter, F., & Barry, C. (2016). Distorted Grids as a Spatial Label and Metric. *Trends in Cognitive Sciences*, *xx*, 2–5. https://doi.org/10.1016/j.tics.2015.12.004

Carpenter, F., Manson, D., Jeffery, K., Burgess, N., & Barry, C. (2015). Grid Cells Form a Global Representation of Connected Environments. *Current Biology*, *25*(9), 1176–1182. https://doi.org/10.1016/j.cub.2015.02.037

Chen, G., Manson, D., Cacucci, F., & Wills, T. J. (2016). Absence of Visual Input Results in the Disruption of Grid Cell Firing in the Mouse. *Current Biology : CB*, 1–8. https://doi.org/10.1016/j.cub.2016.06.043

Crone, G. R. (1953). *Maps and their makers: an introduction to the history of cartography*. Hutchinson's University Library, London, New York.

Daw, N. D., & Dayan, P. (2014). The algorithmic anatomy of model-based evaluation. *Philosophical Transactions of the Royal Society of London. Series B, Biological Sciences*, *369*(1655), 20130478-. https://doi.org/10.1098/rstb.2013.0478

Derdikman, D., Whitlock, J. R., Tsao, A., Fyhn, M., Hafting, T., Moser, M.-B., & Moser, E. I. (2009). Fragmentation of grid cell maps in a multicompartment environment. *Nature Neuroscience*, *12*(10), 1325–1332. https://doi.org/10.1038/nn.2396

Doeller, C. F., Barry, C., & Burgess, N. (2010). Evidence for grid cells in a human memory network. *Nature*, *463*(7281), 657–661. https://doi.org/10.1038/nature08704

Elliott, D. (1987). The influence of walking speed and prior practice on locomotor distance estimation. *Journal of Motor Behavior*, *19*(4), 476–485.

https://doi.org/10.1080/00222895.1987.10735425

Engbert, R., & Kliegl, R. (2003). Microsaccades uncover the orientation of covert attention. *Vision Research*, *43*(9), 1035–1045. https://doi.org/10.1016/S0042-6989(03)00084-1

Epstein, R. A. (2008). Parahippocampal and retrosplenial contributions to human spatial navigation. *Trends in Cognitive Sciences*, *12*(10), 388–396. https://doi.org/10.1016/j.tics.2008.07.004

Erdem, U. M., & Hasselmo, M. E. (2013). A Biologically Inspired Hierarchical Goal Directed Navigation Model. *Journal of Physiology, Paris.* https://doi.org/10.1016/j.jphysparis.2013.07.002

Gibson, J. J. (1958). Visually controlled locomotion and visual orientation in animals. *British Journal of Psychology (London, England : 1953)*, *49*(3), 182–194. https://doi.org/10.1207/s15326969eco103&4_2

Giocomo, L. M., & Hasselmo, M. E. (2008). Computation by oscillations: implications of experimental data for theoretical models of grid cells. *Hippocampus*, *18*(12), 1186–1199. https://doi.org/10.1002/hipo.20501

Hafting, T., Fyhn, M., Molden, S., Moser, M.-B., & Moser, E. I. (2005). Microstructure of a spatial map in the entorhinal cortex. *Nature*, *436*(7052), 801–806. https://doi.org/10.1038/nature03721

Hardcastle, K., Ganguli, S., & Giocomo, L. M. (2015). Environmental Boundaries as an Error Correction Mechanism for Grid Cells. *Neuron*, 1–13. https://doi.org/10.1016/j.neuron.2015.03.039

Horner, A. J., Bisby, J. A., Zotow, E., Bush, D., & Burgess, N. (2016). Grid-like Processing of Imagined Navigation. *Current Biology*, 1–6. https://doi.org/10.1016/j.cub.2016.01.042

Howard, L. R., Javadi, A. H., Yu, Y., Mill, R. D., Morrison, L. C., Knight, R., Loftus, M. M., Staskute, L., & Spiers, H. J. (2014). The Hippocampus and Entorhinal Cortex Encode the Path and Euclidean Distances to Goals during Navigation. *Current Biology*, 1–10. https://doi.org/10.1016/j.cub.2014.05.001

Hutton, C., Josephs, O., Stadler, J., Featherstone, E., Reid, A., Speck, O., Bernarding, J., & Weiskopf, N. (2011). The impact of physiological noise correction on fMRI at 7T. *NeuroImage*, *57*(1), 101–112. https://doi.org/10.1016/j.neuroimage.2011.04.018

Julian, J. B., Keinath, A. T., Frazzetta, G., & Epstein, R. A. (2018). Human entorhinal cortex represents visual space using a boundary-anchored grid. *Nature Neuroscience.* https://doi.org/10.1038/s41593-017-0049-1

Keinath, A. T., Epstein, R. A., & Balasubramanian, V. (2017). Environmental deformations dynamically shift the grid cell spatial metric. *BioRxiv*, 1–13. https://doi.org/http://dx.doi.org/10.1101/174367

Kiani, R., & Shadlen, M. N. (2009). Representation of confidence associated with a decision

1   by neurons in the parietal cortex. *Science (New York, N.Y.)*, *324*(2009), 759–764.

2   https://doi.org/10.1126/science.1169405

3   Killian, N. J., Jutras, M. J., & Buffalo, E. A. (2012). A map of visual space in the primate

4   entorhinal cortex. *Nature*, *5*(December), 3–6. https://doi.org/10.1038/nature11587

5   Knill, D. C., & Pouget, A. (2004). The Bayesian brain: The role of uncertainty in neural

6   coding and computation. *Trends in Neurosciences*, *27*(12), 712–719.

7   https://doi.org/10.1016/j.tins.2004.10.007

8   Kraus, B. J., Brandon, M. P., Robinson, R. J., Connerney, M. A., Hasselmo, M. E., &

9   Eichenbaum, H. (2015). During Running in Place, Grid Cells Integrate Elapsed Time

10   and Distance Run. *Neuron*, *88*(3), 578–589.

11   https://doi.org/10.1016/j.neuron.2015.09.031

12 Krupic, J., Bauza, M., Burton, S., Barry, C., & O'Keefe, J. (2015). Grid cell symmetry is

13   shaped by environmental geometry. *Nature*, *518*(7538), 232–235.

14   https://doi.org/10.1038/nature14153

15 Kubie, J. L., & Fenton, A. a. (2012). Linear Look-Ahead in Conjunctive Cells: An Entorhinal

16   Mechanism for Vector-Based Navigation. *Frontiers in Neural Circuits*, *6*(April), 1–15.

17   https://doi.org/10.3389/fncir.2012.00020

18 Kunz, L., Navarro Schröder, T., Lee, H., Montag, C., Lachmann, B., Sariyska, R., Reuter, M.,

19   Stirnberg, R., Stöcker, T., Messing-Floeter, P. C. C., Fell, J., Doeller, C. F., &

20   Axmacher, N. (2015). Reduced grid-cell-like representations in adults at genetic risk for

21   Alzheimer's disease. *Science*, *350*(6259), 430–433.

22   https://doi.org/10.1126/science.aac8128

23 Manjón, J. V, Coupé, P., Martí-Bonmatí, L., Collins, D. L., & Robles, M. (2010). Adaptive

24   non-local means denoising of MR images with spatially varying noise levels. *Journal of*

25   *Magnetic Resonance Imaging : JMRI*, *31*(1), 192–203.

26   https://doi.org/10.1002/jmri.22003

27 Mathis, A., Herz, A. V. M., & Stemmler, M. (2012). Optimal Population Codes for Space:

28   Grid Cells Outperform Place Cells. *Neural Computation*, *24*(9), 2280–2317.

29   https://doi.org/10.1162/NECO_a_00319

30 Mathis, A., Herz, A. V. M., & Stemmler, M. B. (2013). Multiscale codes in the nervous

31   system: The problem of noise correlations and the ambiguity of periodic scales.

32   *Physical Review E - Statistical, Nonlinear, and Soft Matter Physics*, *88*(2), 1–10.

33   https://doi.org/10.1103/PhysRevE.88.022713

34 McNaughton, B. L., Battaglia, F. P., Jensen, O., Moser, E. I., & Moser, M.-B. (2006). Path

35   integration and the neural basis of the "cognitive map". *Nature Reviews. Neuroscience*,

36   *7*(8), 663–678. https://doi.org/10.1038/nrn1932

37 Meister, M. L. R., & Buffalo, E. A. (2018). Neurons in primate entorhinal cortex represent

gaze position in multiple spatial reference frames. *The Journal of Neuroscience*, *38*(10), 2432–17. https://doi.org/10.1523/JNEUROSCI.2432-17.2018

Nau, M., Navarro Schröder, T., Bellmund, J. L. S., & Doeller, C. F. (2018). Hexadirectional coding of visual space in human entorhinal cortex. *Nature Neuroscience*. https://doi.org/10.1038/s41593-017-0050-8

Navarro Schröder, T., Haak, K. V, Zaragoza Jimenez, N. I., Beckmann, C. F., & Doeller, C. F. (2015). Functional topography of the human entorhinal cortex. *ELife*, *4*(JUNE), 1–17. https://doi.org/10.7554/eLife.06738

Navratilova, Z., Giocomo, L. M., Fellous, J. M., Hasselmo, M. E., & McNaughton, B. L. (2012). Phase precession and variable spatial scaling in a periodic attractor map model of medial entorhinal grid cells with realistic after-spike dynamics. *Hippocampus*, *22*(4), 772–789. https://doi.org/10.1002/hipo.20939

Poser, B. A., Koopmans, P. J., Witzel, T., Wald, L. L., & Barth, M. (2010). Three dimensional echo-planar imaging at 7 Tesla. *NeuroImage*, *51*(1), 261–266. https://doi.org/10.1016/j.neuroimage.2010.01.108

Pouget, A., Beck, J. M., Ma, W. J., & Latham, P. E. (2013). Probabilistic brains: knowns and unknowns. *Nature Neuroscience*, *16*(9), 1170–1178. https://doi.org/10.1038/nn.3495

Power, J. D., Barnes, K. a, Snyder, A. Z., Schlaggar, B. L., & Petersen, S. E. (2012). Spurious but systematic correlations in functional connectivity MRI networks arise from subject motion. *NeuroImage*, *59*(3), 2142–2154. https://doi.org/10.1016/j.neuroimage.2011.10.018

Raudies, F., & Hasselmo, M. E. (2015). Differences in Visual-Spatial Input May Underlie Different Compression Properties of Firing Fields for Grid Cell Modules in Medial Entorhinal Cortex. *PLOS Computational Biology*, *11*(11), e1004596. https://doi.org/10.1371/journal.pcbi.1004596

Sreenivasan, S., & Fiete, I. (2011). Grid cells generate an analog error-correcting code for singularly precise neural computation. *Nature Neuroscience*, *14*(10), 1330–1337. https://doi.org/10.1038/nn.2901

Stangl, M., Achtzehn, J., Huber, K., Dietrich, C., Tempelmann, C., & Wolbers, T. (2018). Compromised Grid-Cell-like Representations in Old Age as a Key Mechanism to Explain Age-Related Report Compromised Grid-Cell-like Representations in Old Age as a Key Mechanism to Explain Age-Related Navigational Deficits. *Current Biology*, 1–8. https://doi.org/10.1016/j.cub.2018.02.038

Stemmler, M. B., Mathis, A., & Herz, A. (2015). Connecting Multiple Spatial Scales to Decode the Population Activity of Grid Cells. *Science Advances*, *in press*(December), 1–12. https://doi.org/10.1126/science.1500816

Stensola, H., Stensola, T., Solstad, T., Frøland, K., Moser, M.-B., & Moser, E. I. (2012). The

entorhinal grid map is discretized. *Nature*, *492*, 72–78. https://doi.org/10.1038/nature11649

Stensola, T., Stensola, H., Moser, M.-B., & Moser, E. I. (2015). Shearing-induced asymmetry in entorhinal grid cells. *Nature*, *518*(7538), 207–212. https://doi.org/10.1038/nature14151

Taube, J. S. (2007). The head direction signal: origins and sensory-motor integration. *Annual Review of Neuroscience*, *30*, 181–207. https://doi.org/10.1146/annurev.neuro.29.051605.112854

Towse, B. W., Barry, C., Bush, D., & Burgess, N. (2014). Optimal configurations of spatial scale for grid cell firing under noise and uncertainty. *Philosophical Transactions of the Royal Society of London. Series B, Biological Sciences*, *369*(1635), 20130290. https://doi.org/10.1098/rstb.2013.0290

United States Department of the Army, . (1996). Tactics, techniques, and procedures for field artillery survey. Headquarters, Department of the Army, Washington, DC.

van Bergen, R. S., Ji Ma, W., Pratte, M. S., & Jehee, J. F. M. (2015). Sensory uncertainty decoded from visual cortex predicts behavior. *Nature Neuroscience*, *18*(12), 1728–1730. https://doi.org/10.1038/nn.4150

Wilber, A. A., Clark, B. J., Forster, T. C., Tatsuno, M., & McNaughton, B. L. (2014). Interaction of Egocentric and World-Centered Reference Frames in the Rat Posterior Parietal Cortex. *Journal of Neuroscience*, *34*(16), 5431–5446. https://doi.org/10.1523/JNEUROSCI.0511-14.2014

Wolbers, T., Wiener, J. M., Mallot, H. A., & Büchel, C. (2007). Differential recruitment of the hippocampus, medial prefrontal cortex, and the human motion complex during path integration in humans. *The Journal of Neuroscience : The Official Journal of the Society for Neuroscience*, *27*(35), 9408–9416. https://doi.org/10.1523/JNEUROSCI.2146-07.2007

Yoshida, W., & Ishii, S. (2006). Resolution of Uncertainty in Prefrontal Cortex. *Neuron*, *50*(5), 781–789. https://doi.org/10.1016/j.neuron.2006.05.006